Mineralogical Magazine (2026), **90**, 427–444
doi:10.1180/mgm.2025.10174

Article

The origin of opal-bearing listvenite from the Tokat region (northern Turkey)

Zeynel Başıbüyük[1], Tomasz Powolny[2], İlkay Kaydu Akbudak[1], Magdalena Dumańska-Słowik[3] and Gökhan Ekıncıoğlu[4]

[1]Department of Geological Engineering, Faculty of Engineering – Architecture, Kırşehir Ahi Evran University, Kırşehir, Türkiye; [2]Institute of Geological Sciences, Jagiellonian University, Krakow, Poland; [3]Faculty of Geology, Geophysics and Environmental Protection, AGH University of Krakow, Krakow, Poland; and [4]Department of Mining and Mineral Extraction, Kaman Vocational School, Kırşehir Ahi Evran University, Kırşehir, Türkiye

Abstract

This study reveals the mineralogy and origin of unusual silica-carbonate bodies (listvenite) associated with tectonized serpentinites and Permian–Triassic phyllites from the Tokat region in northern Turkey. The listvenite includes green-coloured opaline silica intersected by saddle dolomite and minor sulfide mineralization (pyrite, cobaltite and enargite). It also hosts abundant chalcedonic bodies, i.e. agate of bluish to bluish-white colour. Listvenite-hosted opaline silica has been recognized as lussatite, a fibrous birefringent opal-CT variety, with a dominantly 'tridymitic' structure. The green colouration results from discrete, but widely disseminated, Cr-bearing smectite-group minerals, such as volkonskoite and/or Cr-montmorillonite. Chromium, the main colouring agent as determined by element-distribution mapping and visible-light spectroscopy, was probably derived from spinel-group minerals (e.g. chromite), the relics of which mark the presence of an ultramafic protolith. In contrast, the vein agate is composed of length-fast chalcedony, with subordinate quartzine and minor opaline silica, followed by drusy quartz. Its bluish colour appears to be related to scattering effects enhanced by elevated moganite contents (up to 46 wt.%). The observed mineral paragenesis suggests at least a two-stage evolution: (1) early listvenitization marked by carbonate-silica alteration of the host serpentinite together with concomitant sulfide precipitation; and (2) subsequent silicification producing chalcedony (agate) veins under low-temperature conditions, followed by possible dissolution of the earlier saddle dolomite. This evolution reflects complex fluid–rock interactions involving CO_2-rich, Ca-bearing and later Si-rich fluids under fluctuating redox and pH conditions. Hence, the proposed crystallization sequence of the associated mineral assemblage is: sulfides (cobaltite+pyrite+enargite) → saddle dolomite → opal (lussatite) + Cr-smectite → chalcedony (agate). These data provide new insights into the genesis, colouration mechanisms and structural state of Cr-bearing opaline and chalcedonic silica in altered ultramafic terrains.

Keywords: chrome opal; lussatite; agate; chalcedony; saddle dolomite; listvenite

(Received 22 July 2025; revised 30 October 2025; accepted 2 November 2025; Accepted Manuscript published online: 19 November 2025)

Introduction

The terms 'opal' and 'chalcedony' correspond to amorphous and nano-crystalline types of silica ($SiO_2{\cdot}nH_2O$), respectively (Flörke *et al.*, 1991; Čurlík and Forgáč, 1996; Gliozzo, 2019). When viewed optically using cross-polarized light, the former appears isotropic (with common reniform and globular fabrics), whereas the latter is anisotropic, with first-order interference colours typical of quartz, but also marked by peculiar fibrous/bundle-like to spherical arrangements of the crystals. In addition, both types of silica are hydrated and/or hydroxylated, as their structures tend to retain variable amounts of water species, i.e. molecular water (H_2O) and/or silanol-group water (Si–OH), that can occupy pores, interstitial spaces and/or crystal boundaries (Graetsch *et al.*, 1987; Boboň *et al.*, 2011). The total water content (H_2O+Si–OH) is quite variable and ranges from ∼1–2 wt.% in chalcedony and from 2–10 wt.% (up to 20 wt.%) in opaline silica (Graetsch *et al.*, 1985; Day and Jones, 2008; Li *et al.*, 2022; Powolny *et al.*, 2024).

On the basis of X-ray diffraction (XRD) and spectroscopic (Raman and FTIR) characteristics, opaline silica can be subdivided into three main types depending on the degree of its disorder. These include: (1) opal-A (highly disordered/amorphous); (2) opal-C (containing well-crystallized cristobalite); and (3) opal-CT (with stacked tridymite-cristobalite domains) (Jones and Segnit, 1971; Elzea *et al.*, 1994; Ghisoli *et al.*, 2010; Curtis *et al.*, 2019). The nature of opal-CT is the subject of controversy as two different structural models have been proposed, i.e. crystalline and paracrystalline. According to the widely accepted view, opal-CT is made up of

Corresponding author: Tomasz Powolny; Email: tomasz.powolny@uj.edu.pl
Associate Editor: Martin Lee
Cite this article: Başıbüyük Z., Powolny T., Kaydu Akbudak İ., Dumańska-Słowik M. and Ekıncıoğlu G. (2026) The origin of opal-bearing listvenite from the Tokat region (northern Turkey). *Mineralogical Magazine* **90**, 427–444. https://doi.org/10.1180/mgm.2025.10174

disordered interlayering of tridymite and cristobalite units (Flörke, 1955). In turn, the paracrystalline model interprets opal-CT as a disordered material similar to amorphous opal-A, containing only a small volume of crystalline stacking units, mainly of tridymitic nature (Smith, 1998; Wilson, 2014; Curtis *et al.*, 2019). A hypothetical opal-T or -TC is also envisaged (Ghisoli *et al.*, 2010), whilst a low birefringent fibrous (chalcedony-like) variety of opal-CT with pseudo-orthorhombic to orthorhombic symmetry is referred to as lussatite (Mallard, 1890; Jones and Segnit, 1971; Flörke *et al.*, 1990; Schindler *et al.*, 2017; Fröhlich, 2020).

In general, the formation of opaline silica occurs in a wide variety of low-temperature geological settings and can involve both biogenic (diatom- and radiolarian-forming) and non-biogenic activity. The latter can be derived from the circulation of hydrothermal fluids in magmatic to sedimentary rocks, continental weathering, followed by the influx of diluted meteoric waters and precipitation of silica as sinters (geyserites) in the vicinity of hot springs (Chauviré *et al.*, 2017; Pineau *et al.*, 2023). The replacement-related nature of opal has also been asserted for silicified serpentinites and organic materials (e.g. wood) (Lacinska and Styles, 2013; Behera and Nayak, 2023; Mustoe, 2023).

Chalcedonic silica is composed of fibre-aligned α-quartz crystallites (~50–100 nm in size), accompanied by a variable admixture of moganite (Heaney and Post, 1992; Heaney *et al.*, 1994; Schmidt and Fröhlich, 2011). The latter represents a metastable but crystalline polymorph of SiO_2 found in relatively young siliceous deposits, in common association with silicified evaporate sequences (Heaney, 1995). As the XRD and spectroscopic characteristics of chalcedony are nearly identical to those of quartz, its further subdivision into so-called length-fast (LF) and length-slow (LS; also known as quartzine) varieties relies on microscopic observations (Cady *et al.*, 1998; Powolny *et al.*, 2024). These subtypes are marked by the crystallographic *c* axis situated perpendicular and parallel to the fibre elongation, respectively. The LF chalcedony is also characterized by normal (non-twisted) and twisted ('zebraic') characters depending on whether the fibres are twisted or not around the *c* [110] axis. Overall, chalcedony can form not only via the transformation and textural maturation of pristine opaline silica (Kastner *et al.*, 1977), with or without moganite as a transitional phase (El-Hawat *et al.*, 2021), but can also crystallize directly from hydrothermal fluid and/or gel-like medium (Heaney, 1993; French *et al.*, 2013; Howard and Rabinovitch, 2018). Chalcedony represents quite a common hydrothermal- and cementation-related phase in volcanic and sedimentary rocks, where it commonly appears as the multi-coloured banded variety termed agate (Götze *et al.*, 2009; Dumańska-Słowik *et al.*, 2013, 2018; Powolny *et al.*, 2019a; Natkaniec-Nowak *et al.*, 2020; Başibüyük *et al.*, 2023). The coexistence of opal and chalcedony within single agate geodes, though not ubiquitous, has been reported in Moroccan agate deposits (Dumańska-Słowik *et al.*, 2013). Both can act as precursors for the formation of recrystallization-related quartz microtextures, such as feathery and mosaic, respectively (Powolny *et al.*, 2024).

Chalcedony and opal can be colourless, but commonly show red, orange, blue, purple and/or black colours. The colouration mechanisms are linked to the presence of specific solid inclusions (carbonaceous material, chrysocolla, Mn-Fe-oxides, sepiolite, etc.), as well as physical effects such as Mie and Rayleigh scattering (Dumańska-Słowik *et al.*, 2008; Başibüyük, 2018; Götze *et al.*, 2020; Ye and Shen, 2020; Lorenzi *et al.*, 2022; Powolny *et al.*, 2024; Welman-Purchase *et al.*, 2024). These effects can eventually be enhanced/modified by crystallite size and water content. One of the most valuable chalcedonic and opal species involves chrysoprase, prase opal and chrome chalcedony (also known as 'mtorolite' and 'aquaprase'), all are green or green-blue coloured with variable tone and saturation (Eggleton *et al.*, 2011; Başibüyük *et al.*, 2020; Feral, 2022; Monico *et al.*, 2024a, 2024b). Both chrysoprase and prase opal are rich in a Ni-bearing clayey pigment ('kerolite–pimelite', willemseite) and/or Ni grafted on the surface silica minerals (Sojka *et al.*, 2004; Eggleton *et al.*, 2011; Čermáková *et al.*, 2017). They are commonly reported in association with altered ultramafic rocks such as weathered (silicified) serpentinites, saprolites and/or laterites (Shigley *et al.*, 2009; Caucia *et al.*, 2016). In contrast, Cr-rich chalcedony/opal is less common in nature, and its actual colouration mechanism (inclusions vs. extra-framework atom) remains poorly resolved.

In the vicinity of Tokat, a town in northern Turkey, silicification has led to the formation of widespread agate (including the rare surprise-egg type), silicified wood and jasper (Kaydu Akbudak *et al.*, 2021; Başibüyük *et al.*, 2023; Yüzbaşıoğlu and Kaydu Akbudak, 2024). Here we report for the first time the abundance of unusual listvenite rocks hosting the coexisting green-coloured (Cr-bearing) opaline silica, saddle dolomite and sulfide mineralization. Using a combined mineralogical and spectroscopic study, our objective was to resolve the structural state of opal and the nature of the agents responsible for the intricate green colouration. This study also highlights the nature of two-stage hydrothermal silicification–carbonatization in ophiolite-related ultramafic rocks, i.e. listvenitization followed by crystallization of chalcedonic bodies (vein agate), as well as their relevance to geodynamic evolution in the study area.

Geological background

The study area, the Tokat Massif, is part of the South-Central Pontides in northern Turkey and preserves the record of the closure of both Paleo- and Neo-Tethyan ocean basins (Şengör and Yilmaz, 1981; Yilmaz *et al.*, 1997). Here, metamorphic, sedimentary and magmatic rocks belong to three substantial tectonic units, including the Akdağmadeni Group, the Yeşilırmak Group and the Tokat Group (Yilmaz and Yilmaz, 2004; Catlos *et al.*, 2013) (Fig. 1a). The former consists mainly of crustal-derived metamorphic rocks (gneiss, amphibolite, schist, quartzite and marble), which were assembled during the Alpine Orogeny and preserve both regional metamorphism up to amphibolite facies and subsequent dynamic metamorphism (Yilmaz and Yilmaz, 2004). The second unit involves the Cretaceous ophiolitic melange of the North Anatolian Ophiolite Belt (Tekeli, 1981). The Tokat group can be subdivided into the Turhal Metamorphics and Devecidağ Melange. The Turhal Metamorphics consist of a Permian–Triassic metavolcanic-sedimentary succession that has been metamorphosed under greenschist-facies conditions and consists of phyllite, schist, metatuff and metabasite (Yilmaz and Yilmaz, 2004). The Devecidağ Melange includes limestone and ophiolite blocks (Silurian to Triassic) hosted by metaclastic and metavolcanic matrices. The ophiolite blocks, of serpentinized peridotite, are believed to represent the Pre-Liassic component of the ancient oceanic crust (Tekeli, 1981). The serpentinite formation was later overprinted by abundant listvenitization along the Izmir–Ankara–Erzincan Suture Zone (IAESZ) due to the activity of hydrothermal fluids related to the granite intrusions in the vicinity of the study area (Sarifakioglu, 2023). The youngest units in the study area are represented by Eocene–Pliocene sedimentary rocks and Quaternary alluviums (Sümengen, 2013).

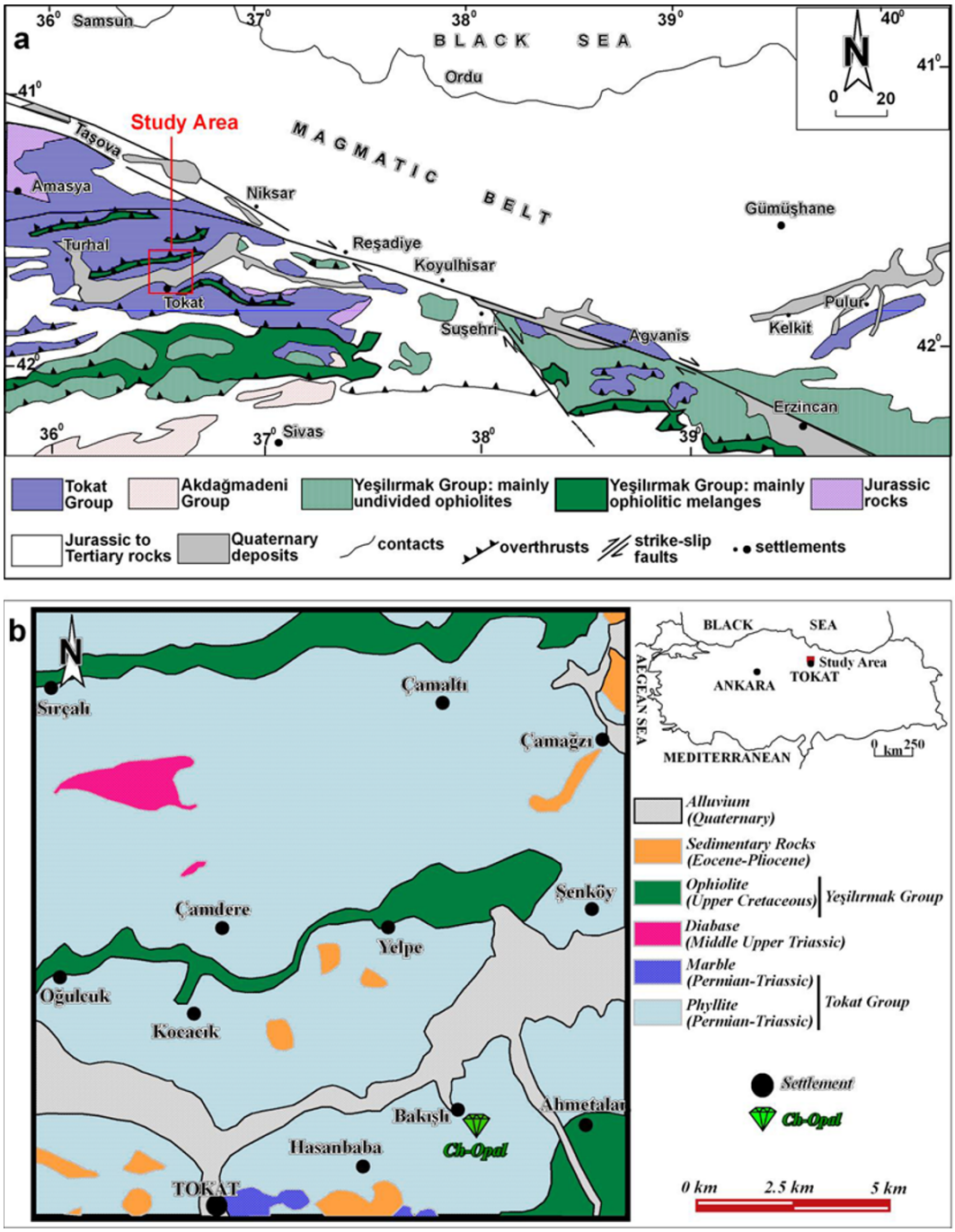

Figure 1. (a) Geological map of northern Turkey in the vicinity of Tokat (modified after Yilmaz and Yilmaz, 2004); (b) main lithologies exposed in the study area together with the locations of sampling sites (modified after Sümengen, 2013).

The opal-bearing listvenite bodies and associated vein agate studied occur within Permian–Triassic phyllites of the Tokat group of the eastern extension of Karakaya complex (Okay and Göncüoğlu, 2004; Tetiker *et al.*, 2015) (Fig. 1b).

Materials and methods

Sample description and field observations

Listvenite-rich bodies are observed as veins reaching 10 cm in width and lenses, up to 1 min length, in the alteration zone of serpentinite located at the tectonic contact with Permian–Triassic phyllites (Fig. 2a–c). Their exposures cover an area of ~0.6 km^2. The rocks analysed feature serpentinite-like (mesh/network-like) fabrics resulting from the presence of numerous white to brownish veins comprising carbonate minerals (dolomite), followed by bluish to bluish-white banded chalcedony (agate) (Fig. 2d). The latter commonly exhibits a botryoidal fabric and can also occur as individual bodies, i.e. not associated with dolomite. Green opal-rich areas appear to be massive, homogeneous and nearly opaque with waxy to oily lustre. Pyrite is visible in hand specimen and

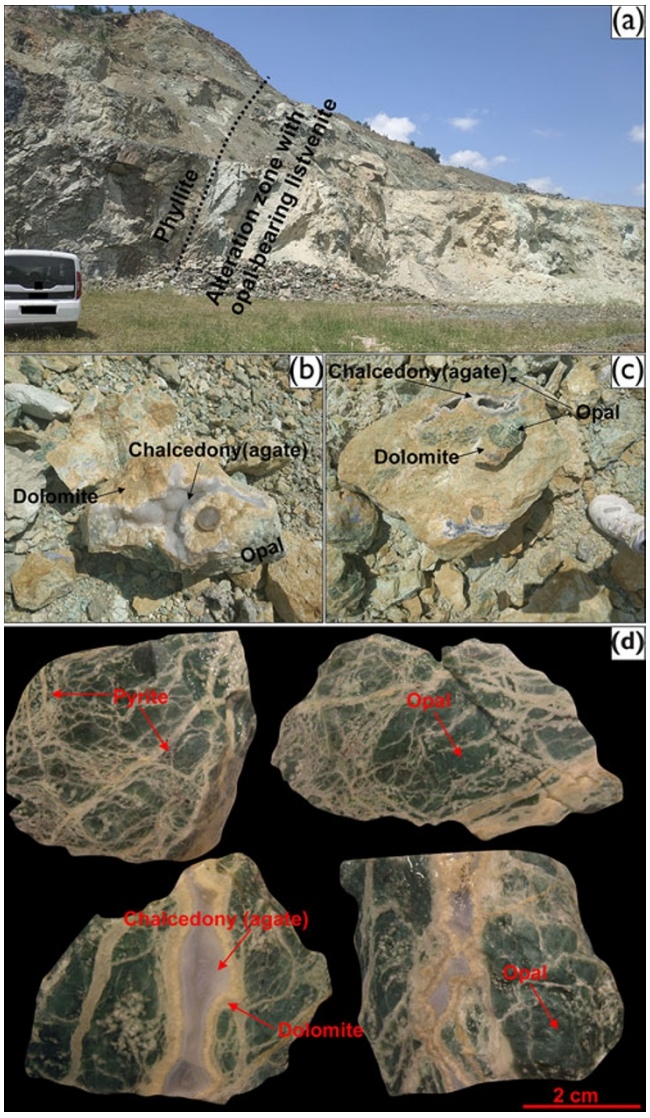

Figure 2. (a) Field exposure and (b–c) field views of green-coloured opal-rich dolomite-bearing listvenite containing agate veins, found in the alteration zone close to the tectonic contact with Permian-Triassic schists (phyllites); (d) a closer view of the listvenite distinguished by serpentinite-like fabrics and the presence of bluish agate veins.

randomly disseminated throughout the opal-rich matrix of listvenite (Fig. 2d).

Analytical techniques

Polarizing microscopy and cathodoluminescence (OM-CL)

Polished thin sections were examined using an Olympus BX-51 polarizing microscope equipped with 4× to 50× objective lenses (Faculty of Geology, Geophysics and Environmental Protection of AGH University of Krakow, Poland). Photomicrographs were taken using an Olympus DP-12 camera combined with *Stream Essential* software. Cathodoluminescence observations were done at the Institute of Earth Sciences (University of Silesia in Katowice, Sosnowiec, Poland), using a CITL Mk5 cold-cathode CL device that operated under 10–15 kV voltage and up to 300 μA current.

Powder X-ray diffraction (PXRD)

Standard PXRD analyses of the powdered opal-rich fragments of listvenite (green colouration) were carried out using a Rigaku SmartLab 9kW X-ray diffractometer (Faculty of Geology, Geophysics and Environmental Protection of AGH University of Krakow, Poland) equipped with curved crystal graphite-monochromatised Cu*K*α radiation (λ = 1.54 Å). The PXRD patterns for air-dried, glycolated and heated (550°C) samples were recorded in the range 2–75°2θ. This was required because of the presence of clay-group species within the opaline silica. The step size, counting time, voltage and current were 0.05°, 1 s/step, 45 kV and 200 mA, respectively. The side-loading method was used during the measurements. Phase identification was provided by *xRayan* (Marciniak and Diduszko, 1994).

Scanning electron microscopy (SEM) supported by electron microprobe analysis (EMPA)

The analyses were undertaken on carbon-coated thin sections, using a JEOL Super Probe JXA-8230 instrument (AGH University of Krakow-KGHM Polska Miedź S.A.) that operated under the following analytical conditions: high-vacuum mode; acceleration voltage of 15 kV; and a beam current of 20 nA. The instrument is equipped with both energy-dispersive (EDS) and wavelength-dispersive spectrometers (WDS). The former was used for preliminary observations and phase identification, whereas the latter provided the composition of dolomite and element-distribution maps.

For dolomite analysis the elements, standards, analytical crystals and detection limits were as follows: Ca – diopside ($CaMgSi_2O_6$), PETJ, 270 ppm; Mg – diopside ($CaMgSi_2O_6$), TAPH, 380 ppm, Fe – hematite (Fe_2O_3); LIFH, 360 ppm; Mn – rhodonite ($CaMn_3MnSi_5O_{15}$), LIFH, 350 ppm; Sr – celestine ($SrSO_4$), PETL, 1900 ppm; and Na – albite ($NaAlSi_3O_8$), TAP, 300 ppm. The peak count time of 10 s, background time of 5 s and beam size of 5 μm were used for WDS measurements.

Element-distribution WDS maps including Ca, Mg, Fe, Al and Cr were obtained from a rectangular area of 280 μm × 345 μm within an opal-rich area, using a 15 kV acceleration voltage and with a dwell time of 100 ms per pixel (i.e. 1 μm × 1 μm). Characteristic *K*α lines of particular elements, measured at PETJ (Ca), TAP (Mg), LIFH (Fe), TAPH (Al) and LIFL (Cr) analytical crystals, were used to determine the semi-quantitative concentration of particular elements.

Raman spectroscopy

The analyses were conducted using a ThermoScientific DXR Raman microscope (Faculty of Geology, Geophysics and Environmental Protection of AGH University of Krakow, Poland) that operated in confocal mode and back-scatter geometry. A laser excitation wavelength of 532 nm was used. The analytical conditions were as follows: 25 μm pinhole, estimated spectral resolution of 3 cm^{-1} and 1 min exposure time. A deconvolution procedure proposed by Götze *et al.* (1998) was applied to establish the concentration of moganite (wt.%), i.e. moganite- and quartz-related bands (501 and 464 cm^{-1}, respectively) were decomposed into two Lorentzian-shaped bands using *OMNIC* Software, followed by a constant background in the range 600–300 cm^{-1}. Subsequently, band integrals $I_{(501)}$

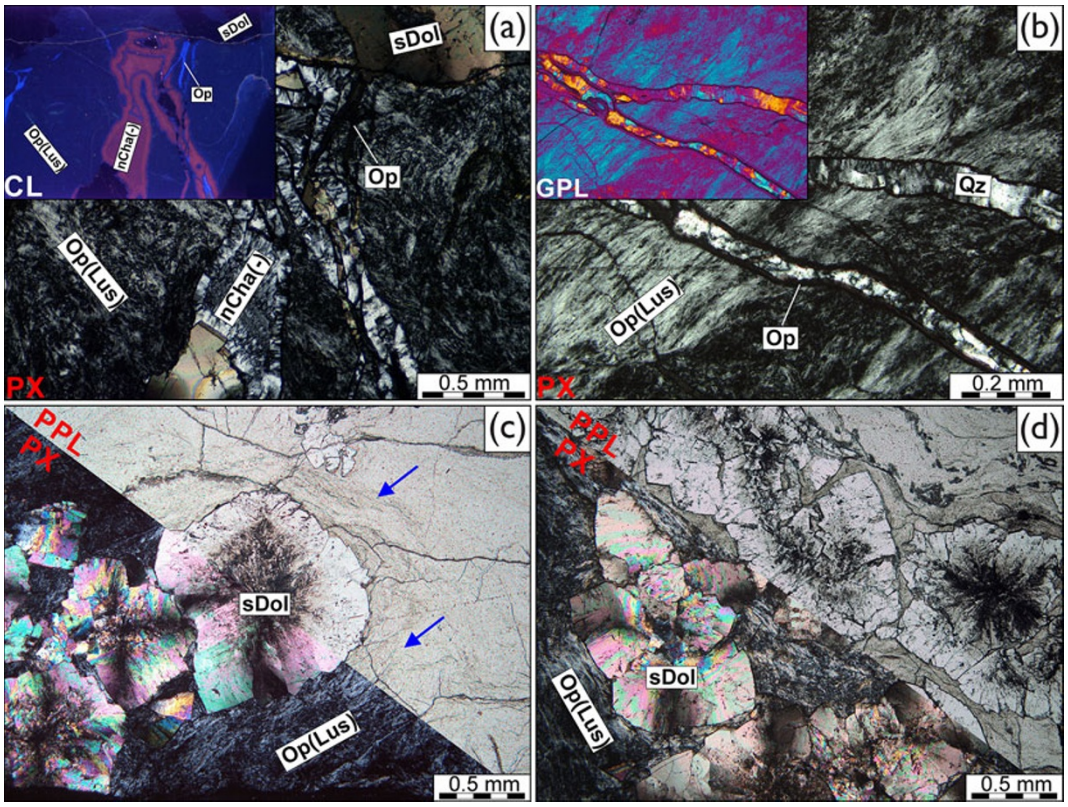

Figure 3. (a) Photomicrograph and the corresponding CL image (inset, upper left) of lussatite-rich (Op-Lus) matrix (green in the macroscale) intersected by saddle dolomite (sDol), non-twisted length-fast (LF) chalcedony (nCha(-)) and another generation of opal (Op) filling the vein in the central part of the image; (b) example of an enlarged view of fibrous opaline silica (lussatite) accompanied by later opal (isotropic) and quartz-rich (Qz) vein. The inset figure, taken with a gypsum-plate inserted from the lower left, accounts for a positive elongation of the fibres. (c,d) Euhedral to subhedral saddle dolomite with cloudy core and limpid rim surrounded by a lussatite-rich matrix. Note the curved (gneiss-like) alignment of opaline silica around larger saddle dolomite (blue arrows). PX – crossed polars; PPL – plane-polarized light; CL – cathodoluminescence; GPL – gypsum plate inserted.

and $I_{(464)}$, referred to as full-width at half-maximum (FWHM), multiplied by the band height, were obtained. The FWHM was also corrected for the specific apparatus prior to the calculations (Irmer, 1985). Finally, the $I_{(501)}/I_{(464)}$ ratios were plotted on the calibration curve provided by Schmidt *et al.* (2013) (Supplementary Fig. S1).

Fourier-transform infrared spectroscopy (FTIR)

The crushed and powdered sample of opaline silica (listvenite-hosted) was analysed in transmission mode using a NICOLET 6700 ThermoScientific instrument (Faculty of Geology, Geophysics and Environmental Protection of AGH University of Krakow, Poland). The ThermoScientific *OMNIC* Software was also used for spectral analysis (e.g. band positions). The analyses were done in ambient conditions, using the potassium bromide (KBr) pellet method, where 200 mg of KBr was mixed with ~3 mg of the sample and then pressed into a transparent pellet. The scanning range, spectral resolution and number of scans were 4000–400 cm^{-1}, 4 cm^{-1} and 64, respectively.

Ultraviolet-Visible-Near Infrared spectroscopy (UV-VIS-NIR)

The analyses were performed using a GemmoSphere UV-VIS-NIR spectrometer located at the Gemological Laboratory of the Faculty of Geology, Geophysics and Environmental Protection of AGH University of Krakow. The acquisition spectra were measured in the range 360–950 nm and used a Xe-boosted light source. The spectral resolution was ~1.3 nm.

X-ray fluorescence

The XRF analyses were performed to determine the major composition of powdered blue chalcedony and opal-dolomite matrix of listvenite samples using a Thermo Brand ARL 2315 Model XRF device at the Geochemistry Laboratory of the General Directorate of Mineral Research and Exploration in Ankara, Turkey.

Inductively Coupled Plasma Mass Spectrometry (ICP-MS)

The ICP-MS analyses were performed to determine the trace element composition of the green opal (listvenite-hosted) and blue chalcedony. The samples were dissolved using perchloric acid ($HClO_4$), hydrofluoric acid (HF), hydrochloric acid (HCl) and nitric acid (HNO_3) and then analysed with the Analytik Jena Brand Plasmaquant MS apparatus located at the General Directorate of Mineral Research and Exploration in Ankara, Turkey.

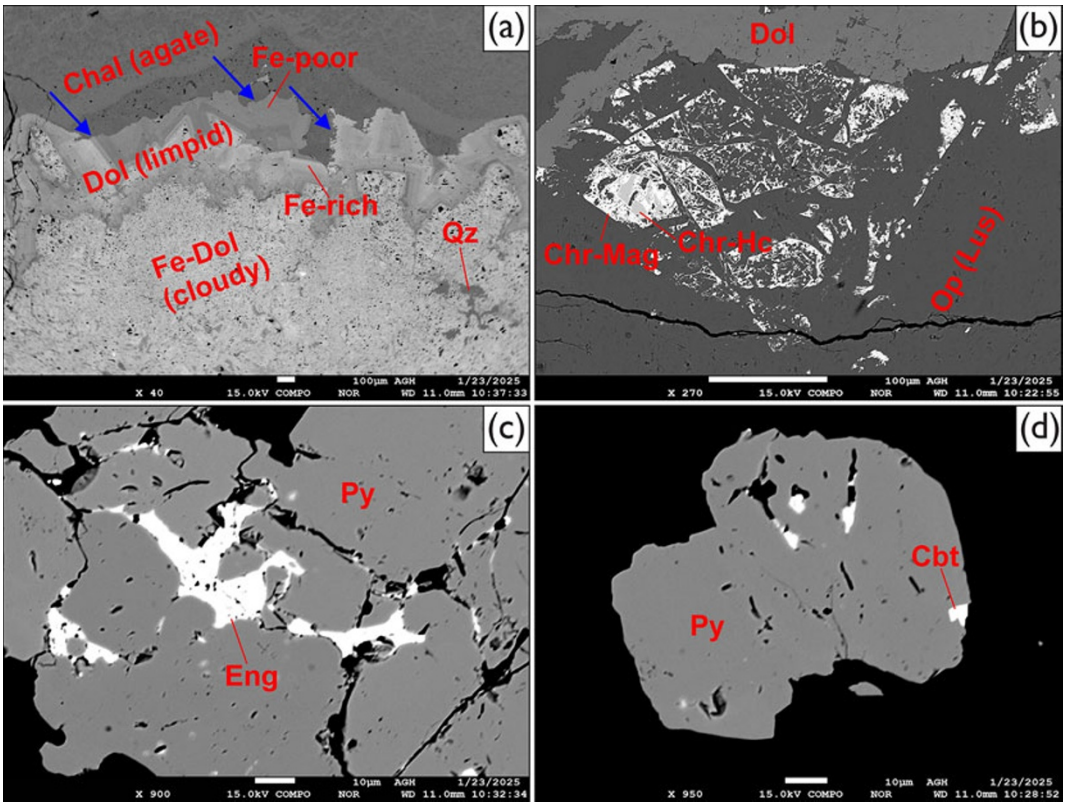

Figure 4. SEM-BSE images of the listvenite samples. (a) The boundary between saddle dolomite and chalcedony (agate) vein. Note the Fe-induced growth-related zonation manifested by dark and light areas, as well as dissolution-erosion-related features that indicate silicification of dolomite (blue arrows). (b) Relics of spinel-group minerals such as chromite-magnetite (Chr-Mag) and chromite-hercynite (Chr-Hc) surrounded by opaline silica and saddle dolomite. (c) Pyrite (Py) hosting an enargite (Eng) inclusion. (d) Pyrite impregnated with cobaltite (Cbt).

Results

Petrography and cathodoluminescence supported by scanning electron microscopy

Opal-rich listvenite exhibits unusual fibrous/filamentous microtextures. In this study, the silica matrix exhibits first-order grey interference colours and positive (+) signs of elongation, coupled with dull blue cathodoluminescence (CL) emission (Fig. 3a,b). The chalcedony-like (i.e. fibrous) appearance of opaline silica indicates the presence of lussatite. The lussatite is further colourless to brownish in plane-polarized light and also tends to mantle larger dolomite crystals (Fig. 3c). Another generation of opaline silica (non-fibrous) occurs as secondary veinlets (up to ~0.1 mm in thickness) with brownish colours and isotropic character, followed by relatively bright-blue CL colours (Fig. 3a). Dolomite is represented by the so-called saddle variety, that is with peculiarly curved crystal faces and sweeping extinction, that reaches ~1 mm in size. The crystals are characterized by roughly rhombohedral habit (Fig. 3c,d), with cloudy non-luminescent cores and limpid, non-luminescent to weak red-luminescent rims. The saddle dolomite commonly has a tabular/elongated morphology where associated with chalcedonic vein-filling silica (agate).

The interior of the dolomite was rich in Fe and relatively abundant in micropores (Fig. 4a), whereas limpid areas revealed oscillatory zonation owing to the variations in Fe and Mn contents. The boundary between dolomite (the external part of the veins cross-cutting the opaline matrix) and agate bodies (innermost regions) displays truncated growth lines and embayed dissolution contacts with silica (Fig. 4a). The opal-rich matrix hosts spinel-group minerals that probably belong to the chromite–magnetite and chromite–hercynite series (Fig. 4b). Pyrite appears to be homogeneous in back-scattered electron (BSE) SEM images but contains minute cobaltite and larger more common enargite inclusions (Fig. 4c,d). The latter were confirmed by Raman spectroscopy as their composition is similar to that of tennantite-Cu.

Chalcedony (agate) veins in opal-bearing listvenite exhibit complex microtextural characteristics, as they contain wall-lining to spherulitic length-fast (LF) chalcedony represented by twisted ('zebraic') and non-twisted ('normal') types, accompanied by only minor amounts of quartzine (length slow) intergrowths (Fig. 5a,b). Prismatic drusy megaquartz (>20 μm; up to ~1 mm in length), as well as very thin (<0.1 mm) opaline bands, are sandwiched between chalcedony-rich regions (Fig. 5c,d). The megaquartz exhibits a local flamboyant appearance, i.e. a crystalline core rimmed by chalcedony. It exhibits both reddish and bluish CL and/or patchy zoning represented by irregular reddish and blue areas within single crystals. Chalcedonic spherules display polygonal fabrics in some places, and also exhibit reddish to pinkish CL emissions. This style of emission is common in nano-crystalline silica and can be assigned to the presence of NBOHC (non-bridging oxygen hole centres) associated with silanol-group water (Götze *et al.*, 1999). As shown in Fig. 5e,f, a single (oval-shaped) chalcedonic (partially recrystallized) spherule illustrates the presence of an irregular rectangular-like zonation pattern resembling growth lines of dolomite. As presented in Fig. 5g,h, chalcedonic silica tends to lose

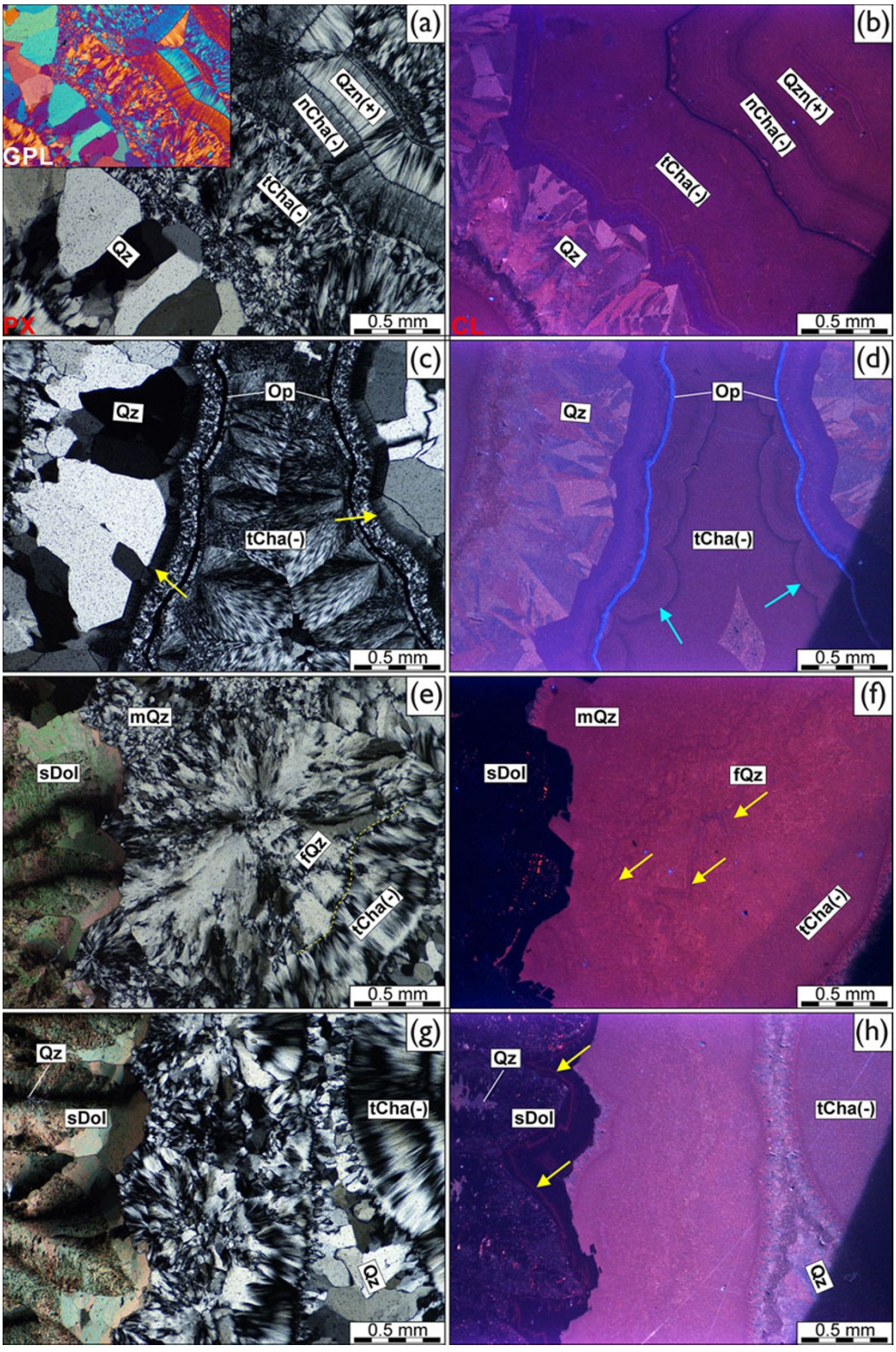

Figure 5. Photomicrographs paired with CL images of chalcedony (agate) and saddle dolomite. (a,b) Megaquartz (Qz) followed by twisted (partially recrystallized) chalcedony (tCha(-)), non-twisted chalcedony (nCha(-)) and quartzine (Qzn(+)). Note the growth-related pattern of chalcedony and patchy zoning of megaquartz visible in CL. The inset photomicrograph (upper left) was taken with a gypsum plate inserted. (c, d) The inner part of chalcedony (agate) vein occluded by megaquartz with flamboyant outline (yellow arrows), opaline silica (blue CL emission) and twisted LF chalcedony with polygonal fabrics (visible under the polarizing microscope). Note that botryoidal fabrics of LF chalcedony revealed by cathodoluminescence (blue arrows) do not conform to polygonal fabrics of chalcedony visible in polarized light. (e,f) Recrystallization of chalcedony (or opal?) into mosaic (mQz) and feathery quartz (fQz) that resulted in the loss of its optically visible fibrosity. Note the presence of a zigzag (rhombic-like) pattern (ghost microtexture of dolomite?) that does not follow the spherulitic arrangement of chalcedony visible under polarizing microscopy (crossed polars) and might have resulted from the replacement of dolomite by silica (yellow arrows). (g,h) The boundary between vein-filling dolomite, followed by a chalcedony (agate) body comprising twisted chalcedony (red CL) and blue luminescent megaquartz. Note the presence of red luminescent growth lines in limpid dolomite (yellow arrows) and quartz penetrating through larger dolomite crystals (upper left).

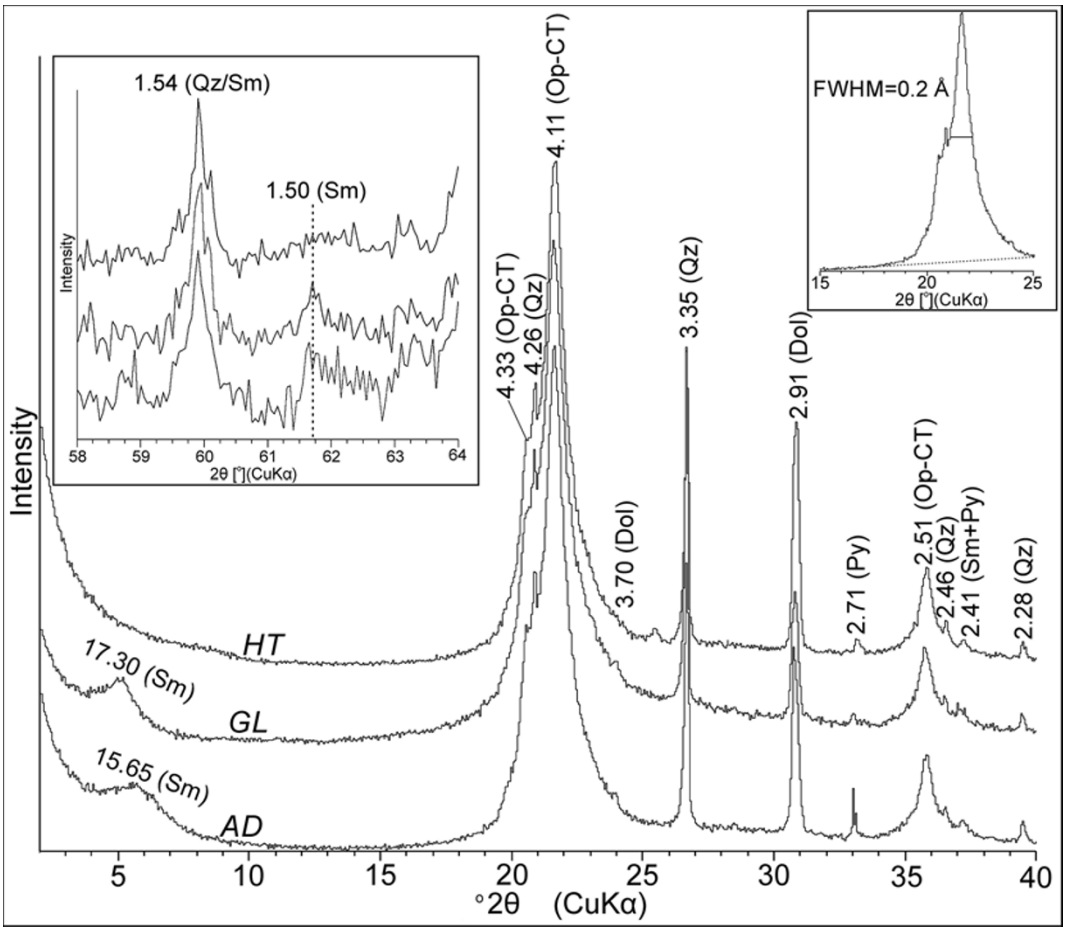

Figure 6. PXRD patterns for the opaline (lussatite-rich) matrix of listvenite in the range of 2–40°2θ, 58–64°2θ (inset image, left) and 15–25°2θ (inset image, right). The full width at half maximum (FWHM) of the main opal-related peak was indicated. The AD, GL and HT symbols refer to the curves obtained for air-dried, glycol-solvated and heated (560°C) powders, respectively. Note the presence of marker peaks for α-quartz (Qz), dolomite (Dol) and pyrite (Py), as well as (001) and (060) reflections of smectite-group clays (Sm), found at 15.65(AD)/17.30(GL) Å and 1.50 Å, respectively.

its microscopically visible fibrosity and transforms into more or less granular quartz, with feathery and/or mosaic (interpenetrating) fabrics.

Powder X-ray diffraction (PXRD)

The PXRD analysis of the green-coloured areas of the listvenite reveals the presence of marker reflections for opal-CT (i.e. 4.33 and 4.11Å), followed by a relatively weak peak at 2.51 Å (Fig. 6). According to the literature (e.g. Elzea *et al.*, 1994; Ilieva *et al.*, 2007; Ghisoli *et al.*, 2010; Fröhlich, 2020), the main XRD peak for opal-CT falls between 4.12 and 4.06 Å and shifts towards lower values, ~4.0 Å, when opal-C becomes a dominant component. The position of the main peak at 4.11 Å, thus marks the presence of highly disordered opal CT with tridymite-dominant characteristics ('Opal-T') (Ghisoli *et al.*, 2010). The full-width at half-maximum (FWHM) of this peak (Fig. 6) attains a relatively low value of 0.2 Å, typical of lussatite, according to Schindler *et al.* (2017). The reflection at 3.35 Å can be assigned to α-quartz. The presence of dolomite and pyrite are proven by the signals at 2.91 and 2.71 Å, respectively. Low-angle regions of the X-ray pattern (below ~10°2θ) reveal a relatively weak but broad peak centred at ~15.65 Å, which shifts towards ~17 Å after saturation with ethylene glycol and collapses due to heating up to 560°C. This observation suggests the presence of swelling clays (i.e. smectite group). The occurrence of minor weak diffraction at 1.50 Å is consistent with its dioctahedral character typical of the montmorillonite–beidellite series (Emmerich, 2013). However, the trioctahedral clay-group species (e.g. saponite) cannot be excluded entirely as its eventual diagnostic peak at 1.54 Å coincides with the quartz-related (211) reflection.

Element-distribution mapping

The distribution of Al, Mg, Fe, Cr and Ca within selected fragments of green-coloured opaline silica (lussatite) elucidated the abundance and character of discrete clay-group species disseminated within it. Even though the given region is still fairly homogeneous under SEM-BSE (with recognizable fibrous/felted microtextures), there is a robust positive correlation among five elements, i.e. Cr, Fe, Mg, Ca and Al (Fig. 7). This type of relationship has confirmed the pigmentation of opaline silica with smectite that has been previously identified via PXRD measurements. As the Cr content appears to be relatively large, this phase can eventually be identified as either volkonskoite (ideally $Ca_{0.3}[CrMgFe]_2[Si,Al]_4O_{10}[OH]_2{\cdot}H_2O$) or a Cr-bearing smectite of the montmorillonite–beidellite series, although direct spot analyses are precluded owing to the small crystal size.

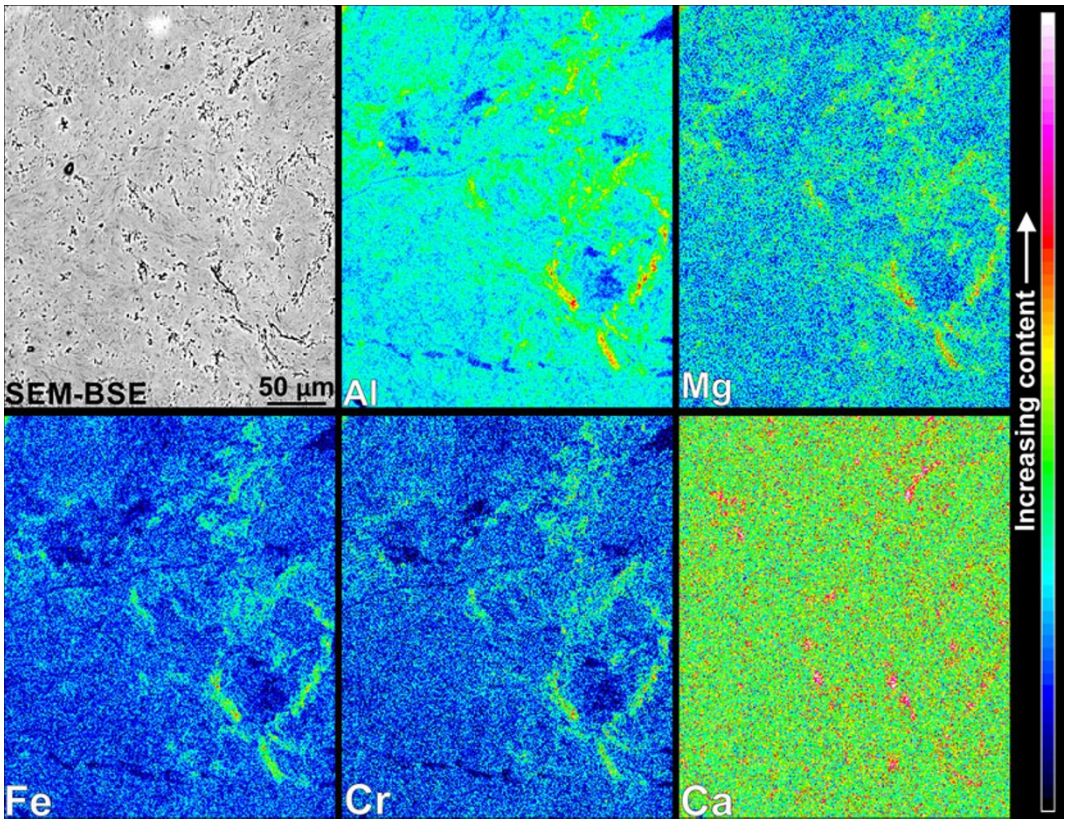

Figure 7. SEM-BSE image and WDS element-distribution maps showing the distribution of Al, Mg, Fe, Cr and Ca in the rectangular area (280 µm × 345 µm) of green-coloured opal (lussatite)-rich matrix of listvenite.

Dolomite composition

The composition of the saddle dolomite is presented in Table 1 and further depicted in an Fe–Mg–Ca ternary diagram (Fig. S2). The inner (cloudy) areas (see Fig. 3c,d), recognized as ferroan dolomite, are enriched in FeO (7.99–9.04 wt.%) with a stoichiometric Ca content (~1.0 atoms per formula unit), coupled with traces of Mn (up to 0.23 wt.%). The empirical formula can be roughly approximated as $Ca_{1.01}(Mg_{0.75}Fe_{0.23}MnO_{0.01})(CO_3)_2$. Limpid outer zones (ferroan to nearly pure dolomite), show variable compositions in terms of both Fe and Mn contents that range between 2.32–8.96 and <0.20 wt.%, respectively. The formula of limpid dolomiteis of a stoichiometric character on the basis of its Ca content (~1.0 apfu), i.e. $Ca_{0.94–1.04}(Mg_{0.79–0.96}Fe_{0.06-0.24}MnO_{0–0.01})(CO_3)_2$. There is also a well-developed positive correlation (R^2 = 0.79) between Fe and Mn contents in the saddle dolomite analysed (Fig. S2).

Table 1. Representative compositions of saddle dolomite (from EMPA) including inner (cloudy) and outer (limpid) areas of the crystals

Type	Cloudy (core)	Limpid (rims)
CL	Non-luminescent	Non-luminescent/red
N	6	14
wt.%	(min.; max); av.	(min.; max); av.
FeO_t	(7.99; 9.04); 8.53	(2.32; 8.96); 4.70
MgO	(15.16; 15.84); 15.42	(16.49; 20.13); 18.02
MnO	(0.19; 0.23); 0.21	(0; 0.20); 0.11
CaO	(28.45; 29.22); 28.92	(26.96; 30.00); 29.21
CO_2*	(44.23; 45.42); 44.89	(45.07; 46.04); 45.55
Total	(96.56; 99.30); 97.96	(96.96; 98.36); 97.60
apfu (based on 6 O)		
Fe	(0.22; 0.25); 0.23	(0.06; 0.24); 0.13
Mg	(0.74; 0.76); 0.75	(0.79; 0.96); 0.86
Mn	(0.01; 0.01); 0.01	(0; 0.01); 0
Ca	(1.01; 1.02); 1.01	(0.94; 1.04); 1.01

*calculated from stoichiometry; apfu – atoms per formula unit

Raman spectroscopy

Examples of Raman spectra obtained for green-coloured opaline silica (lussatite) are presented in Fig. 8 and also mark the presence of opal-CT (Smallwood *et al.*, 1997; Ilieva *et al.*, 2007; Ivanov *et al.*, 2011; Gouzy *et al.*, 2023). There is a strong and broad band centred at ~360 cm^{-1} (with two more or less visible satellite bands at 418 and 265 cm^{-1}) related to O–Si–O bending vibrations, followed by minor bands at 785 and 1063 cm^{-1} that can be both assigned to the symmetric Si–O–Si stretching vibrations (Ivanov *et al.*, 2011). The spectrum in the water-related range (Fig. 8, inset) comprises a broad and asymmetric band between 3800 and 3000 cm^{-1}. This signal originates from water molecules (H_2O) bound by both opaline silica and clay-group species (smectite). The presence of silanol-group water (Si–OH) is supported by the weak band at 965 cm^{-1} (Sodo *et al.*, 2016), although another silanol-related marker signal at 3750 cm^{-1} is absent owing to the possible hydrogen bonding induced by large amounts of molecular water (Gouzy *et al.*, 2023). Finally, the spectrum (Fig. 8) contains a weak band at ~705 cm^{-1},

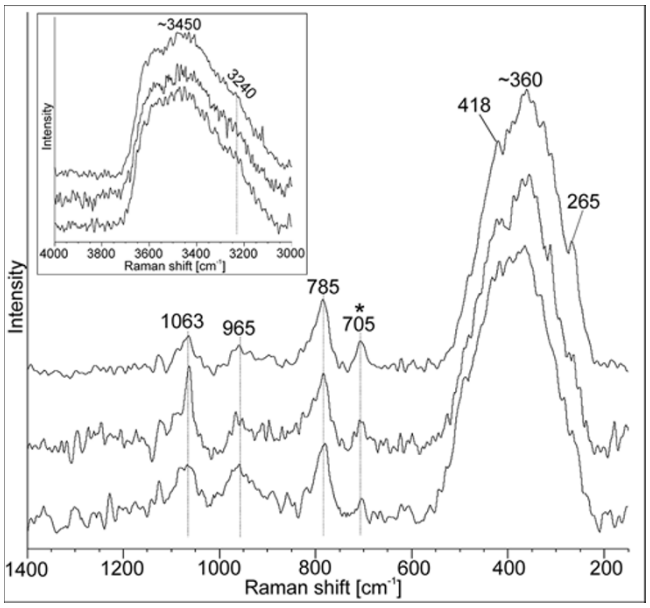

Figure 8. Examples of Raman spectra for green opaline silica (lussatite) of listvenite in the range 1400–150 cm^{-1}. Note that the band at 705 cm^{-1} (*) appears to be due to the smectite impurity. The spectrum in the water-related region (4000–3000 cm^{-1}) is included as an inset (upper left).

which can be attributed to the smectite-group species (e.g. Cr-montmorillonite, volkonskoite). This signal probably arises from Si–O_b–Si vibration modes (b refers to bridging oxygen) of phyllosilicates and chain silicates (Wang *et al.*, 2015).

The most prominent Raman band of lussatite, found at ~360 cm^{-1}, can be further decomposed into at least five sub-bands according to the Voigt function (Fig. 9), with the maxima centred at ~260, ~300, ~360, ~428 and ~485 cm^{-1}. Using the intensity and full-width at half maximum (FWHM) of the decomposed representative spectra (Fig. 9), the so-called ξ and η parameters can be obtained. According to Ilieva *et al.* (2007) and Zhao and Bai (2020), the ξ and η parameters reflect the participation of the tridymite component and the defect concentration of theoretical tridymitic and cristobalitic nanoregions, respectively. As the values of those parameters correspondingly range between 0.97–1.08 and 0.60–0.67, the tridymite component seems to prevail over the cristobalite one, although they probably share a similar degree of defectiveness.

Raman spectra obtained from chalcedonic bands with agate banding reveal the presence of coexisting α-quartz and moganite, the diagnostic bands of which (symmetric stretching-bending modes) appear at 464 cm^{-1} and 501 cm^{-1}, respectively (Kingma and Hemley, 1994). The latter can, however, partially overlap with the band originating from the silanol-group water (Schmidt *et al.*, 2012). According to Fig. 10a–d, at least three zones (1–3) of different hues are tentatively distinguished within single agate bodies, where moganite addition had been estimated in the overall range of 24–46 wt.% (see Materials and Methods for the principles of the deconvolution-based procedure of quartz and moganite-related bands). In particular, the thin bluish zone 1 at the boundary with encasing saddle dolomite shows elevated moganite content (39–45 wt.%), but these values decrease to 24–33 wt.% once the colour shifts from bluish towards bluish-white in the zone 2. The innermost (bluish) regions of agate bodies, referred to as zone 3,

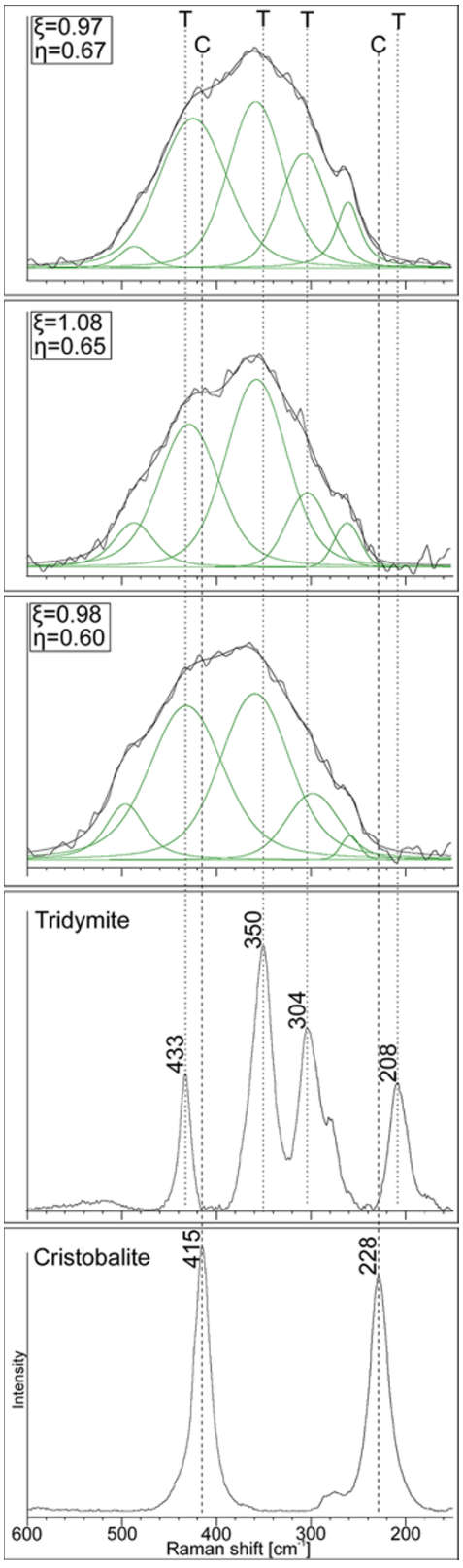

Figure 9. Deconvolution of Raman spectra of opaline silica (lussatite) in the range 600–150 cm^{-1}, followed by the values of so-called ξ and η parameters (see text for further details). The reference spectra of tridymite (T) and cristobalite (C), attached in the lower part of the image, were taken from the *RRUFF* database (Lafuente *et al.*, 2015), i.e. R090042 (tridymite) and R061107 (cristobalite).

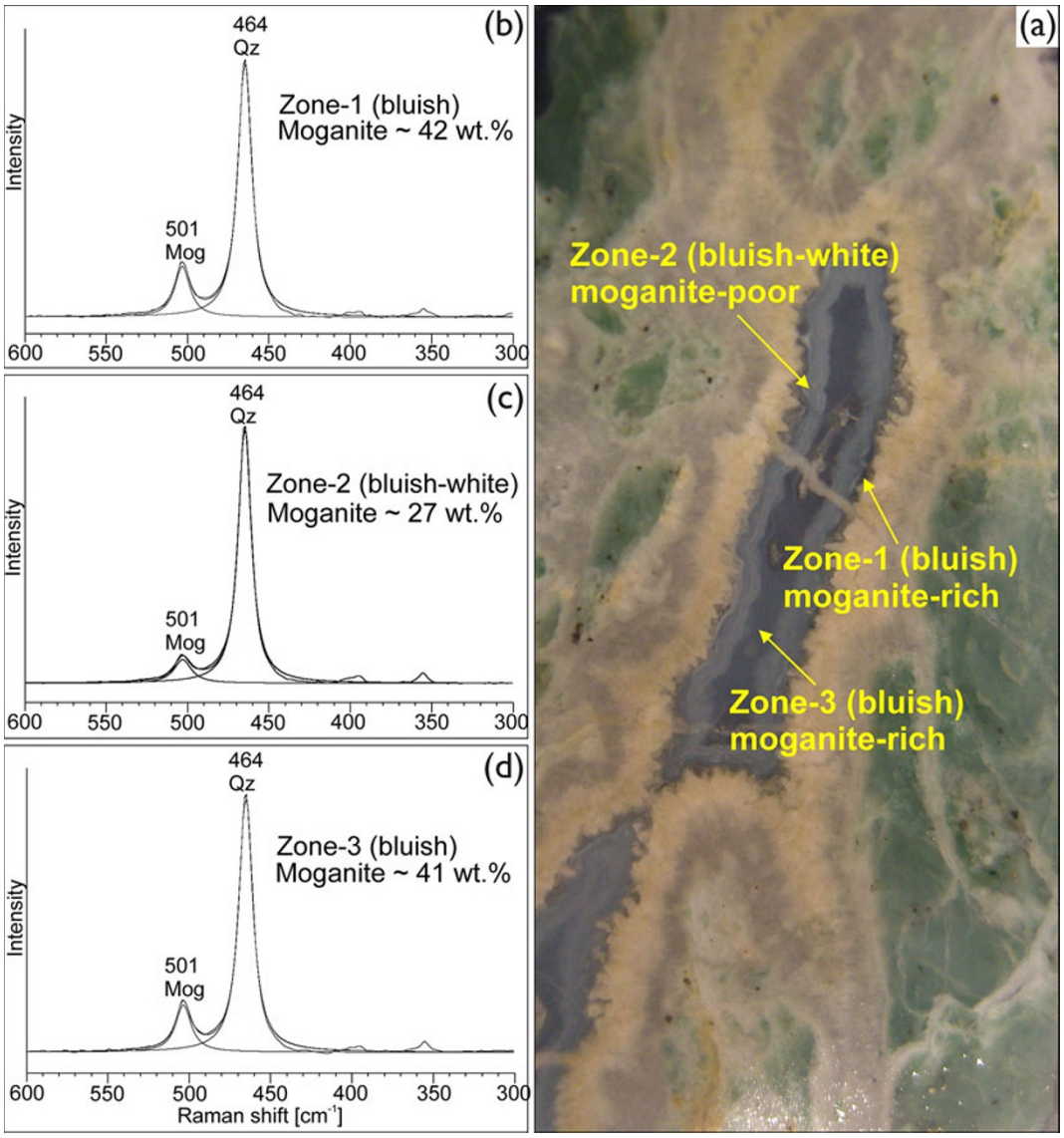

Figure 10. (a) The distribution of moganite-rich (bluish, Zones 1 and 3) and moganite-poor (bluish-white, Zone 2) areas with a single chalcedonic (agate) body surrounded by a dolomite and opal-rich matrix; (b, c, d) average (based on five individual analyses collected from each of the three zones) and deconvoluted spectra and the calculated mean moganite concentration (wt.%).

show an increase in moganite admixture that covers the range 37–46 wt.%.

Raman spectroscopy also confirmed the presence of enargite hosted by the opaline matrix of listvenite (Fig. S3). Here, the strong band at 339 cm^{-1}, accompanied by quite weak signals centred at ~384 and 278 cm^{-1}, was recognized. According to Berkh *et al.* (2023), these bands correspond to As–S vibrations, i.e. antisymmetric stretching, symmetric stretching and bending modes, respectively.

Fourier-transform infrared spectroscopy (FTIR)

The FTIR spectra of green-coloured opaline silica (lussatite) show three prominent main bands centred at 1100, 789 and 474 cm^{-1} (Fig. 11a). These bands can be attributed to fundamental vibrations of the SiO_4 tetrahedral network, i.e. Si–O–Si antisymmetric stretching, Si–O–Si symmetric stretching and O–Si–O bending modes, respectively (Etchepare *et al.*, 1974; Fröhlich, 2020). Weak signals at 1880 and 1631 cm^{-1} are due to overtones of Si–O vibrations and bending of molecular water, respectively. All of these features are consistent with opal-CT characteristics reported elsewhere in the literature (Rice *et al.*, 1995; Adamo *et al.*, 2010; Fröhlich, 2020; Ejigu *et al.*, 2022). Additional bands at 1427, 881 and 728 cm^{-1} originate from stretching and bending modes of the CO_3^{2-} group fixed with dolomite (Hsiao *et al.*, 2019). A weak signal at 671 cm^{-1} can be assigned to the presence of Si–O deformation bands in smectite-group species (Bukka *et al.*, 1992), whereas the band at 694 cm^{-1} marks the presence of trace amounts of α-quartz (impurity or intergrowths) (Fig. 11b). In addition, the water-related region of the spectrum (Fig. 11c) shows a broad band with a maximum at ~3450 cm^{-1} and quite a sharp peak at 3650 cm^{-1}. These signals are linked to the presence of molecular water (H_2O) and silanol-group water (Si–OH), respectively

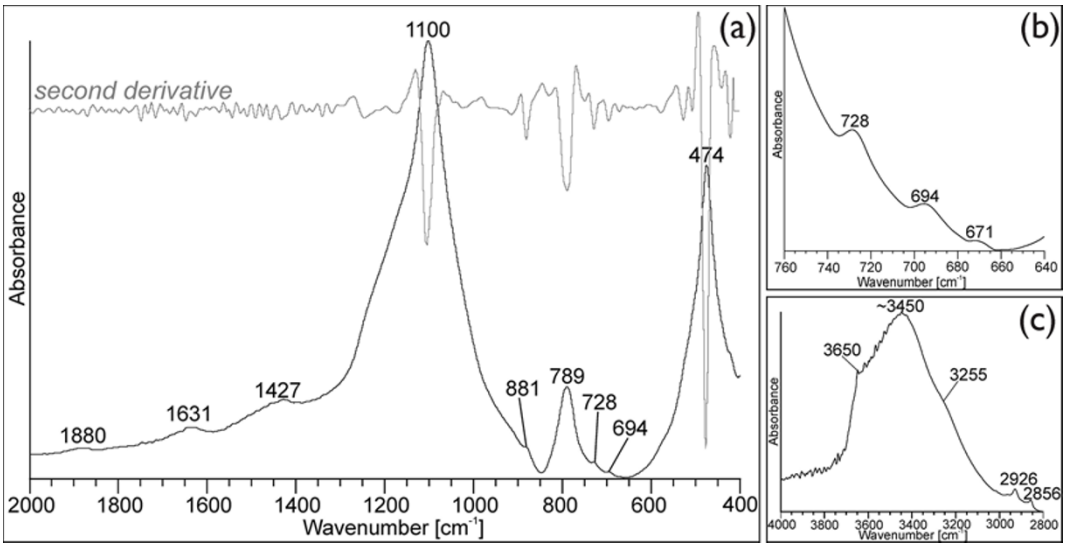

Figure 11. (a) FTIR spectrum collected from green-coloured opaline silica (lussatite) in the range 2000–400 cm^{-1}. The second derivative curve was obtained to unravel eventual discrete quartz-related bands. Note that the shape of this curve is quite similar to that obtained from lussatite termed 'biot opal-CT' in the work of Fröhlich (2020). (b) The same spectrum in the range 760–640 cm^{-1}; (c) water-related region (4000–2800 cm^{-1}) of the FTIR cm^{-1} spectrum where Si–OH and H_2O-related signals at 3650 and 3450 cm^{-1} are presented.

(Graetsch *et al.*, 1985; Flörke *et al.*, 1991), though the spectrum has probably been modified by the vibrations of water molecules hosted by smectite-group species. Two additional but minor bands at 2926 cm^{-1} and 2856 cm^{-1} visible in Fig. 11c reflect vibrations of the methylene group C–H (Ejigu *et al.*, 2022).

Ultraviolet-Visible-Near Infrared (UV-VIS-NIR) spectroscopy

The UV-VIS-NIR spectrum for the analysed green opaline silica (lussatite) has two weak absorption bands at ~450 nm and ~490 nm, followed by a broad and asymmetric signal centred at ~600 nm (Fig. 12). Additionally, there is a small sharp peak centred at 681 nm. These features are consistent with the presence of chromium (Cr^{3+}) in octahedral coordination and were reported for chrome-bearing chalcedony deposits referred to as aquaprase/mtrolite (Willing and Stocklmayer, 2003; Feral, 2022; Lv and Guo, 2023). Such a spectral characteristic is remarkably different compared to chrysoprase (or prase opal), where Ni-bearing hydrous silicates (kerolite–pimelite and/or willemseite) act as colouring agents (Fig. 12). In particular, the spectrum of chrysoprase (added to Fig. 12) exhibits a broad and prominent band at ~650 nm, followed by a shoulder band at ~740 nm. According to Lv and Guo (2023) and Jiang and Guo (2021), this type of spectral characteristic can be assigned to octahedrally-coordinated Ni^{2+} and/or Fe^{2+}-Fe^{3+} charge transfer. Figure 12 also illustrates the UV-VIS-NIR spectrum obtained from bluish chalcedony (agate). The spectrum is relatively flat with absorption at 450 and 482 nm, followed by a broad and diffuse band at ~600 nm, that was reported from moganite-rich bluish chalcedony according to Kiefert *et al.* (2023).

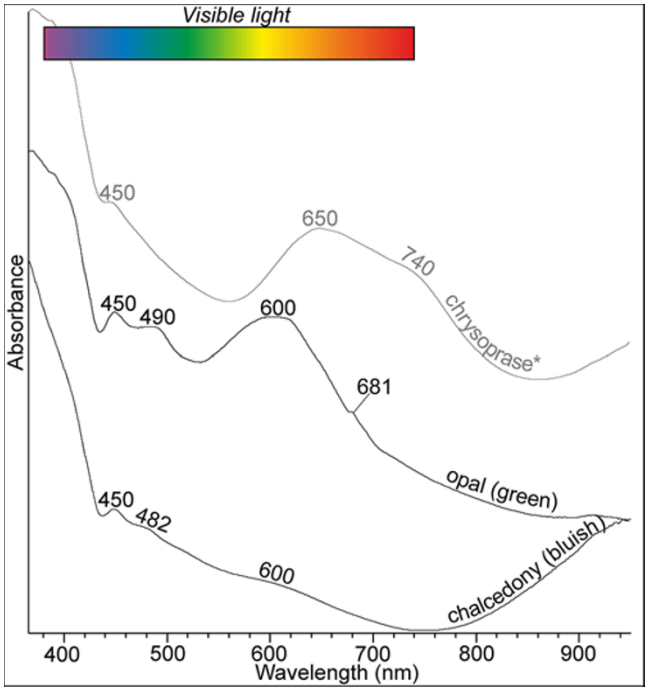

Figure 12. UV-VIS-NIR spectra for green-coloured opaline silica (lussatite) and bluish chalcedony (agate) from the Tokat area. The reference spectrum for chrysoprase from the Szklary area (Lower Silesia, Poland) is shown to emphasise the difference between Cr- and Ni-related colour enhancements.

Whole-rock composition

The juxtaposition of major-element (XRF-based) and trace-element (ICP-MS-based) compositions obtained from the opal-rich listvenite (green) and vein agate (bluish to white) is shown in Table 2. The former contains SiO_2 (53.1 wt.%), with CaO (12.3 wt.%) and MgO (6.7 wt.%) due to the presence of dolomite impurities. Fe_2O_3 and Al_2O_3 reach 5.7 and 1.1 wt.%, respectively, reflecting the presence of dolomite, pyrite and smectite impurities (see the PXRD patterns), whereas the high LOI value (19.90 wt.%) arises from the presence of water-hosted components (opal, smectite) and $[CO_3]^{2-}$ groups fixed with dolomite. The opal-rich listvenite (green) is enriched in transition metals with chromophore

Table 2. Main (XRF-based) and trace (ICP-MS-based) whole-rock element composition of green-coloured opal-rich matrix and vein agate

	Chalcedony (agate)	Opal+dolomite matrix
Main element (wt.%)		
SiO_2	97.1	53.1
CaO	0.3	12.3
MgO	0.1	6.7
Fe_2O_3	0.7	5.7
Al_2O_3	0.1	1.1
MnO	<0.1	0.2
Na_2O	0.1	0.1
K_2O	<0.1	<0.1
P_2O_5	<0	<0.1
TiO_2	<0.1	<0.1
LOI*	1.50	19.90
Total	99.9	99.1
Trace element (ppm)		
As	179.7	121.6
Be	0.6	0.1
Bi	<0.1	0.1
Cd	0.2	0.2
V	6.8	24.1
Cr	62.4	1615.3
Co	6.2	108.1
Ni	24.6	307.3
Cu	11.2	155.4
Zn	9	33
Sn	<10	<10
Ga	1	5.5
Ge	0.5	0.9
Hf	0.5	0.8
In	<0.1	<0.1
Mo	7.3	1.2
Sb	0.2	0.3
Tl	<0.1	<0.1
Pb	5.7	11.1
Th	<2	<2
U	<2	<2

*LOI – loss on ignition

affinities such as: Cr (1615 ppm); Ni (307 ppm); Cu (155 ppm); Mn (1550 ppm); Co (108 ppm); and V (24 ppm), whereas high-field strength elements (U, Th and Hf) are at low and/or below detection limits. The composition of vein agate (blue to white) is dominated by SiO_2 (97.1 wt.%) with the minor FeO (0.7 wt.%) and CaO (0.3 wt.%). Here, the amounts of trace elements are quite low compared with the opal-rich green-coloured matrix, except for significant amounts of As (180 ppm) and Mo (7.3 ppm) (Table 2).

Discussion

Colouring agents and the structural state of opaline and chalcedonic silica

The combined microscopic, PXRD and spectroscopic data argue for the presence of opal-CT (lussatite variety) as the dominant component of the green-coloured opaline matrix of listvenite. The term lussatite was originally coined by Mallard (1890) and refers to the length-slow fibrous opal-CT with hydrothermal origin (Graetsch *et al.*, 1994), but can also serve as a discrete mixture of chalcedony and opal-rich domains (Rogers, 1938). The reported opal-CT (lussatite) shows a more 'tridymitic' nature as evidenced by the position of the FTIR-related band at 789 cm^{-1} close to the tridymite reference at 791 cm^{-1}, as well as the position of the XRD peak at 4.11 Å and the shape of the Raman spectra in the low-wavenumber range.

The green colouration of opaline silica from the Tokat region has been enhanced by the presence of chromium, as evidenced by the shape of the UV-VIS-NIR diagnostic absorption band at 681 nm (Feral, 2022). The presence of Cr at a concentration level of 1615 ppm, was further confirmed using the ICP-MS technique. Note that, Ni and Fe at 307 and 4430 ppm, respectively, could also act as chromophores and/or modify the saturation/tone of the observed green hue. The powder XRD data combined with elemental WDS mapping (Figs 6 and 7, respectively) suggest strongly that Cr and Fe are sequestered in phyllosilicates such as volkonskoite and/or Cr-rich montmorillonite (both green in the macroscale) which act as colouring agents for opaline silica. The reported colouration mechanism is analogous to that reported from chrysoprase, where a green hue was considered to be due to the presence of nickel ions hosted by clay minerals (willemseite and/or kerolite/pimelite) (Sojka *et al.*, 2004; Eggleton *et al.*, 2011; Čermáková *et al.*, 2017). In addition, Cr was probably derived from the breakdown of pristine spinel-group minerals (e.g. chromite), the relics of which were observed in the opaline matrix of listvenite (Fig. 4b).

In contrast, the bluish-white colouration of chalcedonic (agate) veins was facilitated by physical effects such as Rayleigh and/or Mie scattering (Götze *et al.*, 2020; Welman-Purchase *et al.*, 2024), rather than by mineral or elemental impurities. These effects reflect the scattering of light by tiny chalcedony (quartz+moganite) particles of a specific size, but can also be linked to the presence of water species. There is also a positive correlation between the admixture of moganite and the intensity of a blue tint, as presented in Fig. 12 (cf. Kiefert *et al.*, 2023). The shift from bluish towards bluish-white colouration could have been caused by the presence of recrystallization-related microtextures followed by possible loss of water (i.e. feathery and mosaic quartz) (Powolny *et al.*, 2024).

Origin and crystallization sequence

The observed mineral assemblage of listvenite (opal-CT_{LUS} + saddle dolomite + Fe-As-Co-sulfides + chalcedony) reflects the pervasive influx of medium- to low-temperature hydrothermal fluids with fluctuating/evolving compositions and/or pH, as well as a possible boiling-related environment. The latter is supported by the local bladed morphology of dolomite and colloform banding of chalcedonic layers (Moncada *et al.*, 2012). The detailed and assumed crystallization sequence is presented in Fig. 13, whereas more detailed petrogenetic implications are discussed below.

The presence of chromite relics together with secondary Cr-bearing phases (volkonskoite, Cr-montmorillonite), as well as the abundance of transition metals (e.g. Cr, Fe, V, Co, Ni; see Table 2), suggest the presence of an ultramafic precursor (e.g. peridotite, gabbro) that has been later strongly affected by the influx of CO_2-bearing fluids, followed by combined *in situ* two-stage silicification (opalization + formation of chalcedonic bodies) and dolomitization (Foord *et al.*, 1987; Boschi *et al.*, 2009). The reported association of silica+dolomite+pyrite reflects the very final stage of weathering and/or coupled silica-carbonate metasomatism (i.e. listvenitization) of serpentinized ultramafic series (Boskabadi *et al.*, 2020; Menzel *et al.*, 2022a, 2022b, 2024). This process results in the leaching of the main serpentine-hosted elements such as Mg, Si and

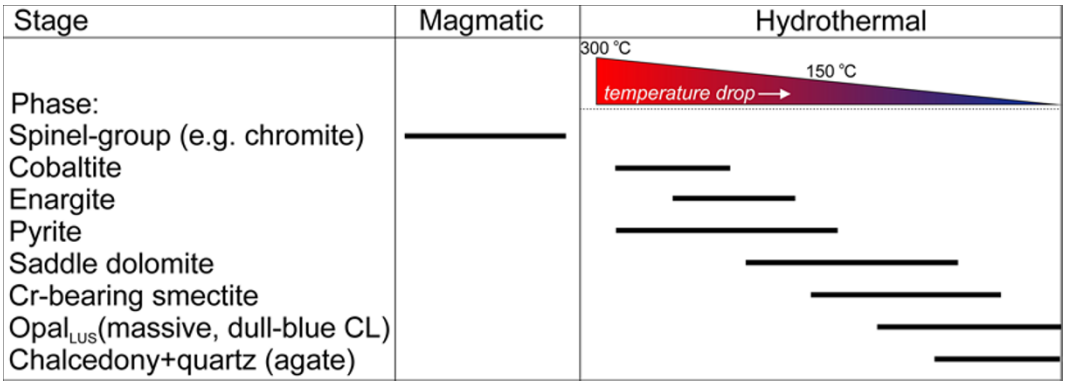

Figure 13. Assumed crystallization sequence of the listevenite accompanied by possible temperature conditions.

Al, whilst Cr, Ni and Fe tend to be immobile during ongoing water–rock interactions (Venturelli *et al.*, 1997; Boschi *et al.*, 2009; Lacinska and Styles, 2013).

Listvenites form below ~200°C and may eventually transform into so-called 'birbirite rocks', where carbonate minerals might have dissolved due to ongoing hydrothermal activity (Menzel *et al.*, 2024). Thus, the stockwork-like macro-texture of the samples (i.e. dolomitic veins intersecting opaline matrix; Fig. 2d) could have been inherited from both serpentinites and listvenites, where carbonate-rich veins (commonly magnesite) are introduced together with the influx of CO_2-rich fluids and the dissolution of serpentinite minerals. As the listvenite analysed does not possess any other unequivocal signs of relic phases (e.g. olivine, serpentinite), and corresponding microtextures (except for chromite remnants), the exact nature of the original rock and silicification mechanisms remains to a certain extent elusive. The proposed petrogenetic hypothesis, however, appears to be valid as ultramafic rocks and their alteration products, belonging to Pre-Liassic and Cretaceous ophiolite complexes (Yilmaz and Yilmaz, 2004; Catlos *et al.*, 2013), are present ubiquitously in the study area. Here, the circulation of hydrothermal Si-rich fluids could be further maintained by the presence of a fault system (e.g. strike-slip faults) and erosional unconformities, although their origin (meteoric, deep-seated hydrothermal?) is vague and requires further analysis (e.g. O and C isotope data). The presence of contrasting (high to medium and low temperature – Fig. 13) mineral assemblages suggests a mixing environment, i.e. the migration of high-temperature metal- and/or CO_2-rich fluids and cooler Ca-rich meteoric waters containing Al and Si. In particular, the sulfide mineralization observed (cobaltite, pyrite, enargite) reflects an early stage of crystallization (possibly exceeding 200°C), followed by the circulation of S-, Fe-, Cu- and As-bearing fluids in the high-sulfidation environment (Dekov *et al.*, 2016; Aluç *et al.*, 2020). Subsequently dolomite veins were introduced, whilst silicification (opalization) and co-crystallization of smectite-group species (Cr-montmorillonite, volkonskoite) postdated or occurred contemporaneously with fracture-filling dolomitization (Menzel *et al.*, 2022a). Syn-kinematic carbonation (i.e. prior to the final silicification/listvenitization) is demonstrated by the deformation of lussatite-rich areas close to adjacent dolomite crystals (Fig. 3c). Dolomite veins could also be partially introduced during late-stage brecciation of already opalized serpentinite. Finally, the two-stage fault-controlled listvenitization, related to either post-granite hydrothermal fluids or meteoric waters, has been discussed widely by Sarifakioglu (2023) in the study of altered ophiolitic series disseminated in the area of Turkey. The coexistence of sulfides (pyrite, cobaltite and enargite) and post-listvenite agate mineralization may thus reflect the presence of both processes during the formation of the rocks analysed.

Two questions remain regarding the proposed origin (i.e. silicification and carbonation of serpentinite) and mineral association (saddle dolomite + opal).

(1) Why was the dolomite formed rather than magnesite, as the latter is far more common in listvenitic rocks (Amarbayar *et al.*, 2023)? This stems from the fact that the magnesite ($MgCO_3$) can readily consume excess Mg released via the dissolution of Mg-bearing silicates of the serpentinite subgroup (chrysotile, antigorite, lizardite), according to the reaction: $Mg_3Si_2O_5(OH)_4 + 3CO_2 = 3MgCO_3 + 2SiO_2 + 2H_2O$ (Amarbayar *et al.*, 2023; Menzel *et al.*, 2024).

(2) Why did the opal (lussatite) crystallize instead of quartz as the latter is more common in the listvenite rocks?

First, the formation of Ca-bearing carbonates (dolomite or calcite) in listvenite-type rocks can be linked to the external influx of $CaCl_2$- and CO_2-rich waters (Menzel *et al.*, 2024) that might have been mixed with serpentinite-related Mg-bearing (residual) fluids, followed by the subsequent invasion of CO_2 (see previous paragraph). Such mixing would reduce Mg/Ca ratios and promote the formation of dolomite, although the *in situ* dissolution of eventual Ca-rich phases (e.g. pyroxene) is still possible to some extent. In addition, the presence of Jurassic–Cretaceous carbonate rocks in the vicinity of the study area (Catlos *et al.*, 2013) could also act as a reservoir for Ca-rich fluids. The alternative scenario involves the replacement of possible pristine magnesite by dolomite (Menzel *et al.*, 2022b), although this hypothesis is not supported by petrographic observations such as pseudomorphic-related textures and remnants of magnesite. Moreover, as the dolomite from the listvenite analysed is chiefly represented by the so-called saddle variety, the influx of hydrothermal fluids between ~60 and 180 °C (Spötl and Pitman, 1998; Davies and Smith, 2006; Zhang *et al.*, 2009) was possible during the listvenitization processes. The distortion of its crystal lattice and peculiar microscopic features (i.e. saddle-shaped crystals, sweeping light extinction) originate from the edge-nucleated crystal growth and significant growth rates, according to Searl (1989). The Na and Sr contents, which are below the detection limit and not listed in Table 1, together with the absence of fluid inclusions suggest that dolomite-forming fluids were of low-salinity and non-evaporitic origin, with the Mg derived from the host serpentinite.

The stoichiometric Ca (~1.0 apfu; Table 1) and high Mn contents of the dolomite analysed, coupled with the large crystal size and common euhedral habit, could point further to a prolonged crystallization from dilute meteoric (or mixed) waters under reducing crystallization conditions. The ferroan nature of dolomite could be enhanced by sulfide (e.g. pyrite) oxidation and subsequent Fe release, with or without the contribution of microbial activity and/or /oxidation of organic materials.

Secondly, the formation of opaline silica (lussatite) rather than quartz suggests the presence of low-temperature, highly silica-supersaturated and polymerized fluids (Fournier, 1985; Boschi *et al.*, 2009). Opalization could also be facilitated by the presence of positively charged hydroxyl complexes (Williams and Crerar, 1985). The origin of lussatite from the Tokat region could be related to either direct precipitation from hydrothermal fluids (Nagase and Akizuki, 1997; Schindler *et al.*, 2017; Mustoe, 2023), or recrystallization from the pristine amorphous opal-A (Ulrich *et al.*, 2014; Liesegang and Tomaschek, 2020). The former scenario is more plausible as there is no petrographic evidence for opal-A to -CT recrystallization, whereas tridymite stacking seems to prevail over cristobalite (note that the latter should be introduced during the textural maturation of opaline silica; Rice *et al.*, 1995). We speculate that the presence of clay-group species has further inhibited the opal-CT→ chalcedony (quartz) transition.

In turn, the formation of chalcedonic (agate) bodies represents the final and low-temperature (post-listvenite) stage of hydrothermal alteration, accompanied by the ongoing reduction in pH and CO_2 activity maintained by the former pervasive crystallization of dolomite. On the basis of microscopic and CL data, there was an inward (syntaxial) growth of chalcedonic bands towards the centre of the vug. Here, chalcedony can be regarded as the product of direct precipitation from fluid, though the observed colloform banding and feathery quartz (see Fig. 5d) might also indicate the presence of an amorphous gel-like precursor (Yilmaz *et al.*, 2016). Moreover, the observed presence of opaline silica between chalcedonic bands (visible in Fig. 5c,d) is not only uncommon in agate deposits worldwide, but can be quite supportive of the rapid changes in silica supersaturation in an agate-forming medium.

The formation of chalcedony (agate) and another generation of opal (i.e. veins crosscutting lussatite; Fig. 3a,b) is probably related to the brecciation of already silicified (opalized) and/or carbonatized serpentinite (listvenite). However, a contemporaneous dissolution of the earlier dolomitic veins by silica should be endorsed based by such petrographic observations as corrosion-related features (Fig. 4a), ghost cathodoluminescence zonation (Fig. 5e,f) and impregnation of dolomite with silica (Fig. 5g–h). Prismatic quartz is commonly observed not only in the centre of chalcedony (agate) bodies, but also in the external regions of the veins (i.e. sandwiched between chalcedonic layers; Fig. 5c,d). This type of sequence is not typical of agate deposits worldwide, where prismatic euhedral quartz tends to occupy the centre of the amygdales/veins due to a progressive decrease in the concentration of dissolved silica (French *et al.*, 2013; Dumańska-Słowik *et al.*, 2018; Powolny *et al.*, 2019b, 2024). Thus, the formation of chalcedonic (agate) veins from the Tokat area originated from remarkable cyclic fluctuations (degree of polymerization and supersaturation, temperature, etc.) of the Si-rich medium. This conclusion is also supported by the local abundance of thin blue-luminescent opal-rich bands between chalcedony-quartz layers, as well as alternating (moganite-rich and moganite-poor) domains (Fig. 10). Furthermore, the presence of moganite (up to 46 wt.%) can be ascribed to the circulation of alkaline fluids (Heaney and Post, 1992; Kayama *et al.*, 2018), but can also be connected with the young age of silica mineralization and lack of pronounced age-related textural maturity (Moxon and Ríos, 2004; Moxon, 2017). Otherwise, the scarcity of LS chalcedony (quartzine) and the preservation of LF chalcedony might suggest an acidic (Mg- and sulfate-poor) crystallization environment (Folk and Pittman, 1971), but the exact controls on the formation of these chalcedony types remains ambiguous (Keene, 1983; Powolny *et al.*, 2024). Finally, the blue CL of prismatic megaquartz is typical of a low-temperature hydrothermal environment during the formation of vein agate (Götze *et al.*, 2009).

Conclusions

(1) There were at least two stages in the formation of opal-bearing listvenite and vein agate from the Tokat area, both related to the circulation of medium- to low-temperature hydrothermal and/or meteoric waters within parental rocks which were possibly serpentinized ultramafics. First, the early post-serpentinite stage (i.e. listvenitization) involved the formation of sulfide mineralization (pyrite, enargite and cobaltite), as well as the crystallization of fracture-filling saddle dolomite and concomitant or later opal–Cr-smectite association. Secondly, the already carbonatized and/or opalized rock (listvenite) was affected by cyclic influxes of Si-rich fluids that precipitated chalcedony (agate) in newly formed vugs, although replacement of the former saddle dolomite by silica should be envisaged. The observed associations suggest the circulation of external CO_2-rich and Ca-rich fluids within Mg-rich parental rock (serpentinite), followed by the later pervasive influx of Si-rich agate-forming solutions.

(2) The green-coloured opaline matrix of listvenite has been recognised as the opal-CT (lussatite subvariety, i.e. with chalcedony-like microfabrics, with a positive sign of elongation) that bears a rather 'tridymitic' than 'cristobalitic' character based on the observed spectroscopic and X-ray diffraction characteristics. The formation of the listvenite was probably related to direct precipitation from supersaturated fluids in a Mg-Ca-Al-rich environment. The cross-cutting chalcedonic (agate) veins consist of α-quartz with a variable moganite admixture (up to 46 wt.%). The latter is responsible for the intensity of a bluish hue within chalcedonic bands but could also maintain recrystallization of silica into mosaic and/or feathery quartz.

(3) The green colour of listvenite-hosted opal-CT (lussatite) is triggered by dispersed Cr-bearing smectite (volkonskoite or Cr-montmorillonite) whilst the chromophore elements (mainly Cr, but also Ni, Fe, Co) were derived from a spinel-bearing ultramafic precursor (serpentinized and now listvenitized). Additionally, the reported colouration mechanism is akin to that reported from chrysoprase, where Ni-bearing clays act as colouring agents. Moreover, Cr-related green colouration produces an exclusive diagnostic UV-VIS-NIR absorption band at ~691 nm, the presence of which is absent from chrysoprase.

Supplementary material. The supplementary material for this article can be found at https://doi.org/10.1180/mgm.2025.10174.

Acknowledgements. This work was supported financially by AGH Statutory Grant No.16.16.140.315. The authors appreciate the assistance of Adam Włodek during the electron microprobe measurements. Peter Heaney and an anonymous reviewer are acknowledged for their comments on the initial version of the text. The authors also thank Principal Editor, Roger Mitchell, for his assistance in handling the manuscript.

Conflict of interest. The Authors declare no conflicts of interest regarding the present work.

References

Adamo I., Ghisoli C. and Caucia F. (2010) A contribution to the study of FTIR spectra of opals. *Neues Jahrbuch für Mineralogie-Abhandlungen*, **187**, 63–68.

Aluç A., Kuşcu İ., Peytcheva I., Cihan M. and von Quadt A. (2020) The late Miocene Öksüt high sulfidation epithermal Au-Cu deposit, Central Anatolia, Turkey: Geology, geochronology and geochemistry. *Ore Geology Reviews*, **126**, 103795.

Amarbayar N., Dandar O., Wang J., Okamoto A., Uno M., Batsaikhan U., Takayanagi H., Iryu Y. and Tsuchiya N. (2023) Progressive carbonation and Ca-metasomatism of serpentinized ultramafic rocks: insights from natural occurrences and hydrothermal experiments. *Contributions to Mineralogy and Petrology*, **178**, 38.

Başibüyük Z. (2018) Mineralogical, geochemical and gemological characteristics of silicic gemstone in Aydıncık (Yozgat-Turkey). *Arabian Journal of Geosciences*, **11**, 292 doi:https://doi.org/10.1007/s12517-018-3615-2.

Başibüyük Z., Akbudak I.K. and Gürbüz M. (2020) Mineralogical, geochemical and gemological investigation of Artova ch-chalcedonies, Tokat – Turkey. *Gospodarka Surowcami Mineralnymi - Mineral Resources Management*, **36**, 77–92.

Başibüyük Z., Gürbüz M. and Kaydu Akbudak İ. (2023) Surprise eggs, the miracle of nature: almus agates (Tokat – Turkiÿe). *Gospodarka Surowcami Mineralnymi/Mineral Resources Management*, **39**, 5–22.

Behera A. and Nayak B. (2023) Metasomatic silicification of chromitite bodies in Asurabandha area, Odisha, India. *Journal of Earth System Science*, **132**, 148.

Berkh K., Majzlan J., Meima J.A., Plášil J. and Rammlmair D. (2023) The effect of chemical variability and weathering on Raman spectra of enargite and fahlore. *European Journal of Mineralogy*, **35**, 737–754.

Boboň M., Christy A.A., Kluvanec D. and Illášová L. (2011) State of water molecules and silanol groups in opal minerals: A near infrared spectroscopic study of opals from Slovakia. *Physics and Chemistry of Minerals*, **38**, 809–818.

Boschi C., Dini A., Dallai L., Ruggieri G. and Gianelli G. (2009) Enhanced CO_2-mineral sequestration by cyclic hydraulic fracturing and Si-rich fluid infiltration into serpentinites at Malentrata (Tuscany, Italy). *Chemical Geology*, **265**, 209–226.

Boskabadi A., Pitcairn I.K., Leybourne M.I., Teagle D.A.H., Cooper M.J., Hadizadeh H., Nasiri Bezenjani R. and Monazzami Bagherzadeh R. (2020) Carbonation of ophiolitic ultramafic rocks: Listvenite formation in the Late Cretaceous ophiolites of eastern Iran. *Lithos*, **352–353**, 105307.

Bukka K., Miller J.D. and Shabtai J. (1992) FTIR study of deuterated montmorillonites: Structural features relevant to pillared clay stability. *Clays and Clay Minerals*, **40**, 92–102.

Catlos E.J., Huber K. and Shin T.A. (2013) Geochemistry and geochronology of meta-igneous rocks from the Tokat Massif, north-central Turkey: Implications for Tethyan reconstructions. *International Journal of Earth Sciences*, **102**, 2175–2198.

Caucia F., Marinoni L., Ghisoli C. and Leone A. (2016) Gemological, physical and chemical properties of prase opals from Hanety Hill (Tanzania). *Periodico di Mineralogia*, **85**, 41–50.

Čermáková Z., Hradil D., Bezdička P. and Hradilová J. (2017) New data on "kerolite-pimelite" series and the colouring agent of Szklary chrysoprase, Poland. *Physics and Chemistry of Minerals*, **44**, 193–202.

Chauviré B., Rondeau B. and Mangold N. (2017) Near infrared signature of opal and chalcedony as a proxy for their structure and formation conditions. *European Journal of Mineralogy*, **29**, 409–421.

Čurlík J. and Forgáč J. (1996) Mineral forms and silica diagenesis in weathering silcretes of volcanic rocks in Slovakia. *Geologica Carpathica*, **47**, 107–118.

Curtis N.J., Gascooke J.R., Johnston M.R. and Pring A. (2019) A review of the classification of opal with reference to recent new localities. *Minerals*, **9**, 299.

Davies G.R. and Smith L.B. (2006) Structurally controlled hydrothermal dolomite reservoir facies: An overview. *American Association of Petroleum Geologists Bulletin*, **90**, 1641–1690.

Day R. and Jones B. (2008) Variations in water content in opal-A and opal-CT from geyser discharge aprons. *Journal of Sedimentary Research*, **78**, 301–315.

Dekov V.M., Rouxel O., Kouzmanov K., Bindi L., Asael D., Fouquet Y., Etoubleau J., Burgaud G. and Wälle M. (2016) Enargite-luzonite hydrothermal vents in Manus Back-Arc Basin: Submarine analogues of high-sulfidation epithermal mineralization. *Chemical Geology*, **438**, 36–57.

Dumańska-Słowik M., Natkaniec-Nowak L., Kotarba M.J., Sikorska M., Rzymetka J.A., Loboda A. and Gaweł A. (2008) Mineralogical and geochemical characterization of the "bituminous" agates from Nowy Kościół (Lower Silesia, Poland). *Neues Jahrbuch fur Mineralogie, Abhandlungen*, **184**, 255–268.

Dumańska-Słowik M., Natkaniec-Nowak L., Wesełucha-Birczyńska A., Gaweł A., Lankosz M. and Wróbel P. (2013) Agates from Sidi Rahal, in the atlas Mountains of Morocco: Gemological characteristics and proposed origin. *Gems and Gemology*, **49**, 148–159.

Dumańska-Słowik M., Powolny T., Sikorska-Jaworowska M., Gaweł A., Kogut L. and Poloński K. (2018) Characteristics and origin of agates from Płóczki Górne (Lower Silesia, Poland): A combined microscopic, micro-Raman and cathodoluminescence study. *Spectrochimica Acta - Part A: Molecular and Biomolecular Spectroscopy*, **192**, 6–15.

Eggleton R.A., Fitz Gerald J. and Foster L. (2011) Chrysoprase from Gumigil, Queensland. *Australian Journal of Earth Sciences*, **58**, 767–776.

Ejigu A.A., Ketemu D.G., Endalew S.A. and Assen W.Y. (2022) Characterization of natural precious opal using modern spectroscopic techniques in Ethiopia: The case from Delanta, South Wollo. *Journal of Spectroscopy*, **2022**, 3194151.

El-Hawat A.S., El-Ghali M.A.K., McLaren S.J. and Kemp S.J. (2021) Early silicification of the Cyrenaican chert, Libya: The importance of moganite as a transitional silicon dioxide phase. *Sedimentology*, **68**, 855–880.

Elzea J.M., Odom I.E. and Miles W.J. (1994) Distinguishing well ordered opal-CT and opal-C from high temperature cristobalite by X-ray diffraction. *Analytica Chimica Acta*, **286**, 107–116.

Emmerich K. (2013) Full Characterization of Smectites. Pp. 381–404 in: *Developments in Clay Science*. 2nd edition. Elsevier, Amsterdam.

Etchepare J., Merian M. and Smetankine L. (1974) Vibrational normal modes of SiO_2. I. α and β quartz. *The Journal of Chemical Physics*, **60**, 1873–1876.

Feral K. (2022) Chromium-bearing translucent green common opal. *Journal of Gemmology*, **38**, 120–122.

Flörke O. (1955) Zur Frage des" Hoch-Cristobalit" in Opalen, Bentoniten und Glasern. *Neues Jahrbuch fur Mineralogie Monatshefte*, 217–224.

Flörke O.W., Graetsch H. and Jones J.B. (1990) Hydrothermal deposition of cristobalite. *Neues Jahrbuch fur Mineralogie. Abhandlungen*, **2**, 81–95.

Flörke O.W., Graetsch H., Martin B., Röller K. and Wirth R. (1991) Nomenclature of micro- and non-crystalline silica minerals based on structure and microstructure. *Neues Jahrbuch für Mineralogie (Abhandlungen)*, **163**, 19–42.

Folk R.L. and Pittman J.S. (1971) Length-slow chalcedony: A New Testament for vanished evaporites. *Journal of Sedimentary Petrology*, **41**, 1045–1058.

Foord E.E., Starkey J.C., Taggart J.E. and Shawe D.R. (1987) Reassessment of the volkonskoite-chromian smectite nomenclature problem. *Clays and Clay Minerals*, **35**, 139–149.

Fournier R.O. (1985) The behavior of silica in hydrothermal solutions. Pp. 45–61 in: *Geology and Geochemistry of Epithermal Systems* (B.R. Berger and P.M. Bethke, editors). Society of Economic Geologists, Inc., Littleton, Colorado, USA.

French M.W., Worden R.H. and Lee D.R. (2013) Electron backscatter diffraction investigation of length-fast chalcedony in agate: Implications for agate genesis and growth mechanisms. *Geofluids*, **13**, 32–44.

Fröhlich F. (2020) The opal-CT nanostructure. *Journal of Non-Crystalline Solids*, **533**, 119938.

Ghisoli C., Caucia F. and Marinoni L. (2010) XRPD patterns of opals: A brief review and new results from recent studies. *Powder Diffraction*, **25**, 274–282.

Gliozzo E. (2019) Variations on the silica theme: Classification and provenance from pliny to current supplies. *European Mineralogical Union Notes in Mineralogy*, **20**, 13–85.

Götze J., Nasdala L., Kleeberg R. and Wenzel M. (1998) Occurrence and distribution of "moganite" in agate/chalcedony: A combined micro-Raman, Rietveld and cathodoluminescence study. *Contributions to Mineralogy and Petrology*, **133**, 96–105.

Götze J., Plötze M., Fuchs H. and Habermann D. (1999) Defect structure and luminescence behaviour of agate — results of electron paramagnetic

resonance (EPR) and cathodoluminescence (CL) studies. *Mineralogical Magazine*, **63**, 149–163.

Götze J., Möckel R., Kempe U., Kapitonov I. and Vennemann T. (2009) Characteristics and origin of agates in sedimentary rocks from the Dryhead area, Montana, USA. *Mineralogical Magazine*, **73**, 673–690.

Götze J., Möckel R. and Pan Y. (2020) Mineralogy, geochemistry and genesis of agate—A review. *Minerals*, **10**, 1037.

Gouzy S., Rondeau B., Gaudin P., Louarn G., La C., Lebeau T., Vinogradoff V., Clodoré L. and Chamard-Bois S. (2023) Whitening of fire opal: Transformation of silica in soils. *Chemical Geology*, **616**, 121237.

Graetsch H., Flörke O.W. and Miehe G. (1985) The nature of water in chalcedony and opal-C from brazilian agate geodes. *Physics and Chemistry of Minerals*, **12**, 300–306.

Graetsch H., Flörke O.W. and Miehe G. (1987) Structural defects in microcrystalline silica. *Physics and Chemistry of Minerals*, **14**, 249–257.

Graetsch H., Gies H. and Topalović I. (1994) NMR, XRD and IR study on microcrystalline opals. *Physics and Chemistry of Minerals*, **21**, 166–175.

Heaney P.J. (1993) A proposed mechanism for the growth of chalcedony. *Contributions to Mineralogy and Petrology*, **115**, 66–74.

Heaney P.J. (1995) Moganite as an indicator for vanished evaporites: a testament reborn? *Journal of Sedimentary Research*, **65**, 633–638.

Heaney P.J. and Post J.E. (1992) The widespread distribution of a novel silica polymorph in microcrystalline quartz varieties. *Science*, **255**, 441–443.

Heaney P.J., Veblen D.R. and Post J.E. (1994) Structural disparities between chalcedony and macrocrystalline quartz. *American Mineralogist*, **79**, 452–460.

Howard C.B. and Rabinovitch A. (2018) A new model of agate geode formation based on a combination of morphological features and silica sol-gel experiments. *European Journal of Mineralogy*, **30**, 97–106.

Hsiao Y.H., Wang B., La Plante E.C., Pignatelli I., Krishnan N.M.A., Le Pape Y., Neithalath N., Bauchy M. and Sant G. (2019) The effect of irradiation on the atomic structure and chemical durability of calcite and dolomite. *NPJ Materials Degradation*, **3**, 36.

Ilieva A., Mihailova B., Tsintsov Z. and Petrov O. (2007) Structural state of microcrystalline opals: A Raman spectroscopic study. *American Mineralogist*, **92**, 1325–1333.

Irmer G. (1985) On the influence of the apparatus function on the determination of scattering cross sections and lifetime from optical phonon spectra. *Experimentalle Technik der Physik*, **33**, 501–506 [in German].

Ivanov V.G., Reyes B.A., Fritsch E. and Faulques E. (2011) Vibrational states in opals revisited. *Journal of Physical Chemistry C*, **115**, 11968–11975.

Jiang Y. and Guo Y. (2021) Genesis and influencing factors of the colour of chrysoprase. *Scientific Reports*, **11**, 1–12. Nature Publishing Group UK.

Jones J.B. and Segnit E.R. (1971) The nature of opal I. Nomenclature and constituent phases. *Journal of the Geological Society of Australia*, **18**, 57–68.

Kastner M., Keene J.B. and Gieskes J.M. (1977) Diagenesis of siliceous oozes-I. Chemical controls on the rate of opal-A to opal-CT transformation-an experimental study. *Geochimica et Cosmochimica Acta*, **41**, 1041–1059.

Kayama M., Tomioka N., Ohtani E., Seto Y., Nagaoka H., Götze J., Miyake A., Ozawa S., Sekine T., Miyahara M., Tomeoka K., Matsumoto M., Shoda N., Hirao N. and Kobayashi T. (2018) Discovery of moganite in a lunar meteorite as a trace of H_2O ice in the Moon's regolith. *Science Advances*, **4**, eaar4378.

Kaydu Akbudak İ., Başıbüyük Z. and Gürbüz M. (2021) Silicified Woods Consist with Malachite, Azurite and Hematite in the Middle Eocene Çekerek Formation, Tokat—Turkey. *Lithology and Mineral Resources*, **56**, 548–558.

Keene J.B. (1983) Chalcedonic quartz and occurrence of quartzine (length-slow chalcedony) in pelagic sediments. *Sedimentology*, **30**, 449–454.

Kiefert L., Krzemnicki M.S., Fiedler J., Sintayehu T. and Furuya M. (2023) Purple to bluish grey chalcedony from Ethiopia. Pp. 67–69 in: *37th IGC 2023 Proceedings - Tokyo, Japan*.

Kingma K.J. and Hemley R.J. (1994) Raman spectroscopic study of microcrystalline silica. *American Mineralogist*, **79**, 269–273.

Lacinska A.M. and Styles M.T. (2013) Silicified serpentinite - A residuum of a Tertiary palaeo-weathering surface in the United Arab Emirates. *Geological Magazine*, **150**, 385–395.

Lafuente B., Downs R.T., Yang H. and Stone N. (2015) The power of databases: The RRUFF project. *Highlights in Mineralogical Crystallography*, **1**, 25.

Li N., Guo Q., Wang Q. and Liao L. (2022) Water characterization and structural attribution of different colored opals. *RSC Advances*, **12**, 30416–30425.

Liesegang M. and Tomaschek F. (2020) Tracing the continental diagenetic loop of the opal-A to opal-CT transformation with X-ray diffraction. *Sedimentary Geology*, **398**, 105603.

Lorenzi R., Zullino A., Gagliardi V., Prosperi L., Paleari A. and Adamo I. (2022) Atomic and microstructural origin of banded colours in purple-blue variety of agate from Yozgat Province, Turkey. *Physics and Chemistry of Minerals*, **49**, 1–8.

Lv H. and Guo Y. (2023) Genesis of the body color of Brazilian gem-quality yellow-green opal. *Crystals*, **13**, 316.

Mallard E. (1890) Sur la Lussatite, nouvelle variété minérale cristallisée de silice. *Bulletin de la Société française de Minéralogie*, **13**, 63–66.

Marciniak H. and Diduszko R. (1994) *XRAYAN: Computer program for X-ray diffraction phase analyzes, version 2.90*. Warsaw, Poland.

Menzel M.D., Urai J.L., Ukar E., Hirth G., Schwedt A., Kovács A., Kibkalo L. and Kelemen P.B. (2022a) Ductile deformation during carbonation of serpentinized peridotite. *Nature Communications*, **13**, 3478.

Menzel M.D., Urai J.L., Ukar E., Decrausaz T. and Godard M. (2022b) Progressive veining during peridotite carbonation: insights from listvenites in Hole BT1B, Samail ophiolite (Oman). *Solid Earth*, **13**, 1191–1218.

Menzel M.D., Sieber M.J. and Godard M. (2024) From peridotite to listvenite – perspectives on the processes, mechanisms and settings of ultramafic mineral carbonation to quartz-magnesite rocks. *Earth-Science Reviews*, **255**, 104828.

Moncada D., Mutchler S., Nieto A., Reynolds T.J., Rimstidt J.D. and Bodnar R.J. (2012) Mineral textures and fluid inclusion petrography of the epithermal Ag-Au deposits at Guanajuato, Mexico: Application to exploration. *Journal of Geochemical Exploration*, **114**, 20–35.

Monico S., Cantaluppi M., Diella V., Gatta G.D., Adamo I., Fumagalli P. and Marinoni N. (2024a) Similarities and differences among selected gemmological varieties of chalcedony: chemistry, mineralogy and microstructure. *Mineralogical Magazine*, **88**, 136–146.

Monico S., Adamo I., Diella V., Melas Y., Prosperi L. and Marinoni N. (2024b) Unveiling the bluish green chalcedony aquaprase™—The study of its microstructure and mineralogy. *Crystals*, **14**, 1003.

Moxon T. (2017) A re-examination of water in agate and its bearing on the agate genesis enigma. *Mineralogical Magazine*, **81**, 1223–1244.

Moxon T. and Ríos S. (2004) Moganite and water content as a function of age in agate: an XRD and thermogravimetric study. *European Journal of Mineralogy*, **16**, 269–278.

Mustoe G.E. (2023) Silicification of Wood: An Overview. *Minerals*, **13**, 206.

Nagase T. and Akizuki M. (1997) Texture and structure of opal-CT and opal-C in volcanic rocks. *The Canadian Mineralogist*, **35**, 947–958.

Natkaniec-Nowak L., Dumańska-Słowik M., Gaweł A., Łatkiewicz A., Kowalczyk-Szpyt J., Wolska A., Milovská S., Luptáková J. and Ładoń K. (2020) Fire agate from the Deer Creek deposit (Arizona, USA) – new insights into structure and mineralogy. *Mineralogical Magazine*, **84**, 343–354.

Okay A.I. and Göncüoğlu C. (2004) The Karakaya Complex: A review of data and concepts. *Turkish Journal of Earth Sciences*, **13**, 77–95.

Pineau M., Chauviré B. and Rondeau B. (2023) Near-infrared signature of hydrothermal opal: a case study of Icelandic silica sinters. *European Journal of Mineralogy*, **35**, 949–967.

Powolny T., Dumańska-Słowik M., Sikorska-Jaworowska M. and Wójcik-Bania M. (2019a) Agate mineralization in spilitized Permian volcanics from "Borówno" quarry (Lower Silesia, Poland) – microtextural, mineralogical and geochemical constraints. *Ore Geology Reviews*, **114**, 103130.

Powolny T., Dumańska-Słowik M., Sikorska-Jaworowska M. and Wójcik-Bania M. (2019b) Agate mineralization in spilitized Permian volcanics from "Borówno" quarry (Lower Silesia, Poland) – microtextural, mineralogical and geochemical constraints. *Ore Geology Reviews*, **114**, 103130.

Powolny T., Dumańska-Słowik M., Szczerbowska-Boruchowska M. and Woszczyna M. (2024) Water and moganite participation in agates from Bou Hamza (Morocco). *Scientific Reports*, **14**, 22473.

Rice S.B., Freund H., Huang W.L., Clouse J.A. and Isaacs C.M. (1995) Application of Fourier transform infrared spectroscopy to silica diagenesis: the opal-A to opal-CT transformation. *Journal of Sedimentary Research A: Sedimentary Petrology & Processes*, **A65**, 639–647.

Rogers A. (1938) Fossil termite pellets in opalized wood from Santa Maria, California. *American journal of science*, **5**, 389–392.

Sarifakioglu E. (2023) Geochemistry and origin of listwaenites within the Northern Branch of Neo-Tethyan ophiolites, Turkey. *Journal of African Earth Sciences*, **197**, 104748.

Schindler M., Fayek M., Courchesne B., Kyser K. and Hawthorne F.C. (2017) Uranium-bearing opals: Products of U-mobilization, diffusion and transformation processes. *American Mineralogist*, **102**, 1154–1164.

Schmidt P. and Fröhlich F. (2011) Temperature dependent crystallographic transformations in chalcedony, SiO_2, assessed in mid infrared spectroscopy. *Spectrochimica Acta - Part A: Molecular and Biomolecular Spectroscopy*, **78**, 1476–1481.

Schmidt P., Bellot-Gurlet L., Slodczyk A. and Fröhlich F. (2012) A hitherto unrecognised band in the Raman spectra of silica rocks: Influence of hydroxylated Si-O bonds (silanole) on the Raman moganite band in chalcedony and flint (SiO_2). *Physics and Chemistry of Minerals*, **39**, 455–464.

Schmidt P., Bellot-Gurlet L., Leá V. and Sciau P. (2013) Moganite detection in silica rocks using Raman and infrared spectroscopy. *European Journal of Mineralogy*, **25**, 797–805.

Searl A. (1989) Saddle dolomite: a new view of its nature and origin. *Mineralogical Magazine*, **53**, 547–555.

Şengör A.C. and Yilmaz Y. (1981) Tethyan evolution of Turkey: A plate tectonic approach. *Tectonophysics*, **75**, 181–241.

Shigley J., Laurs B. and Renfro N. (2009) Chrysoprase and prase opal from Haneti, Central Tanzania. *Gems and Gemology*, **45**, 271–279.

Smallwood A.G., Thomas P.S. and Ray A.S. (1997) Characterisation of sedimentary opals by Fourier transform Raman spectroscopy. *Spectrochimica Acta - Part A: Molecular and Biomolecular Spectroscopy*, **53**, 2341–2345.

Smith D.K. (1998) Opal, cristobalite and tridymite: Noncrystallinity versus crystallinity, nomenclature of the silica minerals and bibliography. *Powder Diffraction*, **13**, 2–19.

Sodo A., Casanova Municchia A., Barucca S., Bellatreccia F., Della Ventura G., Butini F. and Ricci M.A. (2016) Raman, FT-IR and XRD investigation of natural opals. *Journal of Raman Spectroscopy*, **47**, 1444–1451.

Sojka Z., Witkowski S., Zabiński W., Dyrek K. and Bidzińska E. (2004) TPR, EPR and UV-Vis studies of Ni(II) speciation in chrysoprase. *Neues Jahrbuch fur Mineralogie, Monatshefte*, **2004**, 11–25.

Spötl C. and Pitman J.K. (1998) Saddle (baroque) dolomite in carbonates and sandstones: A reappraisal of a burial-diagenetic concept. *Carbonate Cementation in Sandstones*, **26**, 437–460.

Sümengen M. (2013) *Scale geological maps of Türkiye, No:188 Tokat - H 37 sheet*.

Tekeli O. (1981) Subduction complex of pre-Jurassic age, northern Anatolia, Turkey. *Geology*, **9**, 68–72.

Tetiker S., Yalçın H., Bozkaya Ö. and Göncüoğlu M.C. (2015) Metamorphic evolution of the Karakaya Complex in northern Turkey based on phyllosilicate mineralogy. *Mineralogy and Petrology*, **109**, 201–215.

Ulrich M., Muñoz M., Guillot S., Cathelineau M., Picard C., Quesnel B., Boulvais P. and Couteau C. (2014) Dissolution-precipitation processes governing the carbonation and silicification of the serpentinite sole of the New Caledonia ophiolite. *Contributions to Mineralogy and Petrology*, **167**, 952.

Venturelli G., Contini S., Bonazzi A. and Mangia A. (1997) Weathering of ultramafic rocks and element mobility at Mt. Prinzera, Northern Apennines, Italy. *Mineralogical Magazine*, **61**, 765–778.

Wang A., Freeman J.J. and Jolliff B.L. (2015) Understanding the Raman spectral features of phyllosilicates. *Journal of Raman Spectroscopy*, **46**, 829–845.

Welman-Purchase M., Wicht J., Miller D. and Roelofse F. (2024) Blue lace agate and chalcedony pseudomorphs from Ysterputs in southern Namibia. *Journal of African Earth Sciences*, **212**, 105211.

Williams L. and Crerar D. (1985) Silica Diagenesis, II. General Mechanisms. *Journal of Sedimentary Petrology*, **55**, 312–321.

Willing M.J. and Stocklmayer S.M. (2003) A new chrome chalcedony occurrence from Western Australia. *The Journal of Gemmology*, **28**, 265–279.

Wilson M.J. (2014) The structure of opal-CT revisited. *Journal of Non-Crystalline Solids*, **405**, 68–75.

Ye M. and Shen A.H. (2020) Gemmological and mineralogical characteristics of chrysocolla chalcedony from Taiwan, Indonesia and the USA and their separation. *Journal of Gemmology*, **37**, 262–280.

Yilmaz A. and Yilmaz H. (2004) Geology and structural evolution of the Tokat Massif (Eastern Pontides, Turkey). *Turkish Journal of Earth Sciences*, **13**, 231–246.

Yilmaz T.I., Duschl F. and Di Genova D. (2016) Feathery and network-like filamentous textures as indicators for the re-crystallization of quartz from a metastable silica precursor at the Rusey Fault Zone, Cornwall, UK. *Solid Earth*, **7**, 1509–1519.

Yilmaz Y., Serdar H.S., Genc C., Yigitbas E., Gürer F., Elmas A., Yldirim M., Bozcu M. and Gürpinar O. (1997) The geology and evolution of the Tokat massif, south-central Pontides, Turkey. *International Geology Review*, **39**, 365–382.

Yüzbaşıoğlu T.Y. and Kaydu Akbudak İ. (2024) Mineralogical characteristics and their usability as gemstones of jaspers in altered metavolcanics belonging to the Topçam Formation, Tokat, Turkiye. *Minerals*, **14**, 1072.

Zhang J., Hu W., Qian Y., Wang X., Cao J., Zhu J., Li Q. and Xie X. (2009) Formation of saddle dolomites in Upper Cambrian carbonates, western Tarim Basin (northwest China): Implications for fault-related fluid flow. *Marine and Petroleum Geology*, **26**, 1428–1440.

Zhao K. and Bai F. (2020) Crystallinity and play-of-colour in gem opal with digit patterns from Wegel Tena, Ethiopia. *Minerals*, **10**, 625.